Modelling of propagating instabilities in pseudoelastic NiTi tubes under combined tension–torsion: helical bands and apparent yield locus*

Mohsen Rezaee-Hajidehi[a], Stanisław Stupkiewicz[a,*]

[a]*Institute of Fundamental Technological Research (IPPT), Polish Academy of Sciences, Pawińskiego 5B, 02-106 Warsaw, Poland.*

Abstract

This paper is concerned with modelling of propagating instabilities and transformation patterns in NiTi tubes subjected to combined tension–torsion loading. A recently developed gradient-enhanced finite-strain model of pseudoelasticity is employed for this purpose, and respective finite-element computations are carried out. It is shown that the model is capable of representing a number of experimentally observed effects. The major effect, which has not been successfully modelled to date, is that the transformation is inhomogeneous under tension-dominated loading and alters towards a homogeneous transformation as the level of torsion is increased. To capture this effect, the model must deliver a non-monotonic (up-down-up) stress–strain response in tension and a monotonic one in torsion, and this can be achieved if the model includes three features: tension–compression asymmetry, transverse isotropy of the transformation strain, and deformation-dependent hardening/softening response. A detailed study is also carried out regarding the transformation yield locus. The results reveal an ambiguity in determination of the yield locus for tension-dominated loading and hence an ambiguity in determination of the tension–compression asymmetry. This aspect seems to have been overlooked in the literature despite its impact on correct interpretation of experimental results.

Keywords: shape memory alloys, phase transformation, strain localization, finite-element method

1. Introduction

One of the superior thermomechanical properties of shape memory alloys (SMAs) is pseudoelasticity, which refers to the ability of the material to recover large inelastic deformations upon unloading. The basic intrinsic mechanism of pseudoelasticity is the reversible stress-induced martensitic phase transformation that takes place between the parent phase (austenite) and the product phase

*Published in *Int. J. Solids Struct.* **221**, 130–149, 2021, doi: 10.1016/j.ijsolstr.2020.09.011

*Corresponding author.

Email addresses: mrezaee@ippt.pan.pl (Mohsen Rezaee-Hajidehi), sstupkie@ippt.pan.pl (Stanisław Stupkiewicz)

(martensite) and is accompanied by formation and evolution of microstructures (Bhattacharya, 2003).

Evolution of the stress-induced martensitic transformation in pseudoelastic NiTi varies depending on geometry and loading. Under uniaxial tension, the transformation typically initiates by a deformation instability in the form of localized martensite bands. The transformation advances then by propagation of interfaces (macroscopic transformation fronts) that separate the transformed and untransformed regions. The associated mechanical response reveals a stress drop followed by a stress plateau. Note that such a response represents the overall response of the specimen, while the intrinsic material response is non-monotonic, i.e. it is characterized by a softening-like branch (up-down-up response), as illustrated by Hallai and Kyriakides (2013), see also Alarcon et al. (2017).

In NiTi strips under uniaxial tension, the instability manifests itself in the form of an inclined martensite band or multiple bands that propagate throughout the specimen, sometimes in a criss-cross pattern, resembling the Lüders bands (e.g. Shaw and Kyriakides, 1997b; Pieczyska et al., 2006; Zhang et al., 2010). In NiTi tubes, the instability occurs via nucleation of a helical martensite band that evolves into a cylindrical domain possessing ring-shaped or prong-like transformation fronts (e.g. Li and Sun, 2002; Sun and Li, 2002; Feng and Sun, 2006; Bechle and Kyriakides, 2014, 2016; Reedlunn et al., 2014, 2020a).

In contrast to uniaxial tension, the martensitic transformation in NiTi under uniaxial compression or shear is usually not characterized by macroscopic instabilities. It has been observed in a handful of experiments that NiTi exhibits homogeneous transformation under compression or shear, and the respective stress–strain response is monotonic. As an exception, a mild inhomogeneity of transformation under shear, not observed previously, has been recently[1] reported by Reedlunn et al. (2020a), see a more detailed discussion below. Moreover, the transformation stress in uniaxial compression is higher compared to that in uniaxial tension, while the transformation strain in compression is smaller, and those of shear lie in between (e.g. Orgéas and Favier, 1998; Sun and Li, 2002; Grabe and Bruhns, 2009; Mao et al., 2010; Bechle and Kyriakides, 2014; Reedlunn et al., 2014, 2020a). Concluding, the experimental observations indicate a significant tension–compression asymmetry (and also tension–shear asymmetry) of NiTi in terms of the mechanical response and in terms of homogeneity of transformation.

Some experimental efforts have been also devoted to study the patterns of propagating instabilities in NiTi under bending or mixed-type loading conditions. For instance, diamond-shaped patterns have been observed in NiTi tubes under bending (Bechle and Kyriakides, 2014; Reedlunn et al., 2014). The effect of initial torsion on the transformation pattern in NiTi tubes under com-

[1]The paper of Reedlunn et al. (2020a) was published after the present paper was submitted to the journal, and the references to that paper were added while revising the manuscript during the review process.

bined tension–torsion has been investigated by Sun and Li (2002). It has been reported that, as the level of the initial torsion increases, the transformation pattern alters from a propagating instability to a homogeneous transformation. The latter conclusion has not been supported by detailed snapshots of the transformation patterns in combined tension–torsion, and only the snapshots of the transformation patterns under uniaxial tension and pure torsion have been provided by Sun and Li (2002). The transition from a propagating instability to a nearly homogeneous transformation has been also observed in NiTi tubes under combined tension and internal pressure (Bechle and Kyriakides, 2016). It is generally agreed that the tension–compression asymmetry contributes to the evolution of the transformation patterns. For instance, the diamond-shaped patterns are only observed in the tensioned side of the NiTi tube under bending. Likewise, due to the tension–shear asymmetry, the transformation tends to be homogeneous as the initial torsion is increased in the case of the NiTi tube subjected to combined tension–torsion.

A qualitatively different behaviour of NiTi tubes under combined tension–torsion has been recently reported by Reedlunn et al. (2020a). Proportional (in the strain space) loading paths have been studied, and the overall stress–strain response has been shown to follow the usual trends: stress plateaus (indicating a non-monotonic material response) in tension-dominated cases and monotonic stress–strain response in torsion- and compression-dominated cases. However, in contrast to the current understanding, the transformation under torsion-dominated loading, including pure torsion, is accompanied by strain localization, as revealed by full-field DIC (digital image correlation) measurements. Quite surprisingly, the instabilities leading to strain localization are not evidenced in the overall stress–strain response which is smooth and monotonic. Moreover, the localization bands are approximately aligned with the tube axis (and are quite diffuse), while a simple reasoning would suggest that ring-like band perpendicular to the tube axis should be preferable. A definite explanation of these effects is currently lacking even if some suggestions have been provided by Reedlunn et al. (2020a).

Note that many experiments have been conducted on pseudoelastic NiTi under combined loading conditions, however, most of the works in this vein are focused on the mechanical response and on the transformation yield stress locus (see e.g. Helm and Haupt, 2003; Sun and Li, 2002; McNaney et al., 2003; Lexcellent and Blanc, 2004; Grabe and Bruhns, 2009; Bechle and Kyriakides, 2016; Reedlunn et al., 2020a), while the respective transformation patterns have been rarely documented, and the main related contributions are those of Sun and Li (2002), Bechle and Kyriakides (2016), and Reedlunn et al. (2020a).

Modelling of deformation localization and propagating instabilities in SMAs is not a new subject of study. The main challenge is to treat the ill-posedness of the boundary value problem that results from the softening-like constitutive behaviour. Accordingly, suitable regularization approaches have

been developed in recent years. Regularization can be achieved by enhancing the model with higher gradient terms, typically, with the gradient of the volume fraction of martensite (e.g. Duval et al., 2011; Badnava et al., 2014; Alessi and Bernardini, 2015; Rezaee-Hajidehi and Stupkiewicz, 2018), including the phase-field-type approaches (e.g. He and Sun, 2010; Wendler et al., 2017), or with the strain gradient (e.g. Chang et al., 2006). As an exception, simulations of the transformation patterns in NiTi strips and tubes have been successfully performed by taking advantage of only the natural 3D regularization effects (Jiang et al., 2017a,b,c; Xiao and Jiang, 2020). A review of the available regularization approaches is not attempted here, see Rezaee-Hajidehi and Stupkiewicz (2018) and Rezaee-Hajidehi et al. (2020) for the related discussion.

Generally, the computational studies of propagating instabilities and transformation patterns are essentially limited to SMA wires, strips and tubes under uniaxial tension (e.g. Chang et al., 2006; He and Sun, 2009, 2010; Jiang et al., 2017b,c; Rezaee-Hajidehi and Stupkiewicz, 2018; Rezaee-Hajidehi et al., 2020), whereas the transformation patterning in other types of loading has been scarcely addressed. As far as we are aware, the only reported example is the simulation of the diamond-shaped transformation patterns in NiTi tubes under bending (Jiang et al., 2017a), which has been accomplished by including a correct tension–compression asymmetry into the model, see also the very recent study of Frost et al. (2020).

The present work is motivated by the experiment of Sun and Li (2002) on NiTi tubes subjected to combined tension–torsion. In particular, it has been observed in the experiment that transformation is inhomogeneous under uniaxial tension and under tension-dominated loading, and the respective transformation pattern is that of a helical band of martensite that subsequently evolves towards a cylindrical domain. On the other hand, the transformation is fairly homogeneous under torsion-dominated loading. To the best of our knowledge, the related effects have not been successfully modelled yet, and thus the main aim of the present work is to study the transformation patterns in NiTi tubes under combined tension–torsion. Analysis of the results of the respective simulations has led us to an interesting observation regarding the apparent transformation yield locus in the case when the transformation under tension-dominated loading is inhomogeneous and the associated overall pseudoelastic response is characterized by a stress drop followed by a stress plateau. The related ambiguity concerning the tension–compression asymmetry of the transformation stress seems to have been overlooked in the literature, and hence an additional study focused on the apparent yield locus is performed here.

The model employed in this work originates from the local isothermal model of pseudoelasticity developed by Stupkiewicz and Petryk (2013). The gradient-enhanced thermomechanically coupled version of the model has been developed by Rezaee-Hajidehi and Stupkiewicz (2018), as well as its 3D extension by Rezaee-Hajidehi et al. (2020). To facilitate the finite-element implementation,

a micromorphic-type regularization of the gradient-enhanced model has been applied, for more details regarding the micromorphic regularization see Forest (2009), see also Mazière and Forest (2015); Ryś et al. (2020) for recent applications of the micromorphic approach in gradient plasticity. The ability of the model to account for tension–compression asymmetry, transverse isotropy of the transformation strain and deformation-dependent hardening/softening response are the distinctive features that allow to capture the complex transformation patterns under combined tension–torsion loadings.

The paper is organized as follows. In Section 2, the gradient-enhanced model and its formulation in the incremental energy minimization framework are presented along with specification of the constitutive functions and extended discussion of the details particularly important for the present study. The finite-element implementation of the model is presented in Section 3, including the micromorphic regularization, the thermomechanical coupling and the details of the finite-element treatment. Analysis of the NiTi tube under combined tension–torsion is carried out in Section 4, accompanied by a detailed study of the transformation yield locus.

2. Gradient-enhanced finite-strain model of pseudoelasticity

The origin of the gradient-enhanced model presented in this section is the local isothermal model of pseudoelasticity developed by Stupkiewicz and Petryk (2013), where the details of the respective constitutive description and of the energy minimization framework can be found. In the present study, some small (but potent) improvements of the constitutive functions are employed. For the details regarding the gradient enhancement and the improved constitutive functions, the reader is referred to Rezaee-Hajidehi et al. (2020).

2.1. Kinematics and basic assumptions

The total deformation gradient $\boldsymbol{F} = \nabla\boldsymbol{\varphi}$, where $\boldsymbol{\varphi}$ is the mapping from the reference configuration to the current configuration, is multiplicatively decomposed into the elastic part $\boldsymbol{F}^{\mathrm{e}}$ and the transformation part $\boldsymbol{F}^{\mathrm{t}}$,

$$\boldsymbol{F} = \boldsymbol{F}^{\mathrm{e}}\boldsymbol{F}^{\mathrm{t}}, \qquad \boldsymbol{F}^{\mathrm{t}} = \boldsymbol{R}^{\mathrm{t}}\boldsymbol{U}^{\mathrm{t}}, \qquad \boldsymbol{U}^{\mathrm{t}} = \exp \boldsymbol{e}^{\mathrm{t}}, \tag{1}$$

where the transformation part $\boldsymbol{F}^{\mathrm{t}}$ is expressed in terms of the transformation stretch tensor $\boldsymbol{U}^{\mathrm{t}}$ and the rotation tensor $\boldsymbol{R}^{\mathrm{t}}$, and $\boldsymbol{R}^{\mathrm{t}} = \boldsymbol{I}$ is assumed so that $\boldsymbol{F}^{\mathrm{t}} = \boldsymbol{U}^{\mathrm{t}}$. Adopting the configuration of undeformed austenite as the reference configuration, we have $\boldsymbol{F}^{\mathrm{t}} = \boldsymbol{I}$ for pure austenite state. It is also justifiably presumed that the martensitic transformation is isochoric, leading to $\det \boldsymbol{F}^{\mathrm{t}} = \det \boldsymbol{U}^{\mathrm{t}} = 1$.

In Eq. (1), the transformation stretch tensor $\boldsymbol{U}^{\mathrm{t}}$ is defined in terms of the logarithmic transformation strain tensor $\boldsymbol{e}^{\mathrm{t}}$ (cf. Stupkiewicz and Petryk, 2013). Following the presumption of isochoric

martensitic transformation, $\boldsymbol{e}^{\mathrm{t}}$ is restricted to be traceless, $\operatorname{tr}\boldsymbol{e}^{\mathrm{t}} = 0$, thus automatically satisfying the condition $\det \boldsymbol{F}^{\mathrm{t}} = 1$. In the stress-induced transformation, the martensite variants are preferably oriented with respect to the local stress. Accordingly, focusing on the pseudoelastic regime, it is assumed here that the martensite is fully oriented. The transformation strain $\boldsymbol{e}^{\mathrm{t}}$ can thus be defined in terms of the transformation strain tensor of the fully oriented martensite, denoted by $\bar{\boldsymbol{e}}^{\mathrm{t}}$, and the volume fraction of martensite, denoted by η, thus

$$\boldsymbol{e}^{\mathrm{t}} = \eta\bar{\boldsymbol{e}}^{\mathrm{t}}, \qquad 0 \leq \eta \leq 1, \qquad \bar{\mathcal{P}} = \{\bar{\boldsymbol{e}}^{\mathrm{t}}\colon\ g(\bar{\boldsymbol{e}}^{\mathrm{t}}) = 0\}. \tag{2}$$

Here, $\bar{\mathcal{P}}$ denotes the set of limit transformation strains and function g is defined such that $g(\boldsymbol{0}) < 0$, $g(\bar{\boldsymbol{e}}^{\mathrm{t}}) = 0$ is a smooth, closed and convex surface in the deviatoric space, and $g(r\bar{\boldsymbol{e}}^{\mathrm{t}})$ is a continuously increasing function of r for $r > 0$ and $\bar{\boldsymbol{e}}^{\mathrm{t}} \neq \boldsymbol{0}$. The explicit form of function g is specified in Section 2.4.

2.2. The energy minimization framework

Following Rezaee-Hajidehi et al. (2020), the isothermal Helmholtz free energy function is adopted in the form

$$\phi(\boldsymbol{F}, \bar{\boldsymbol{e}}^{\mathrm{t}}, \eta, \nabla\eta) = \phi_0(\eta) + \phi_{\mathrm{el}}(\boldsymbol{F}, \bar{\boldsymbol{e}}^{\mathrm{t}}, \eta) + \phi_{\mathrm{int}}(\bar{\boldsymbol{e}}^{\mathrm{t}}, \eta) + \phi_{\mathrm{grad}}(\nabla\eta), \tag{3}$$

where ϕ_0 represents the so-called chemical energy, ϕ_{el} the elastic strain energy, ϕ_{int} the interaction energy and ϕ_{grad} the gradient energy term. The individual components of ϕ are specified in Section 2.3.

The functional of the global potential energy reads

$$\mathcal{E}[\boldsymbol{\varphi}, \bar{\boldsymbol{e}}^{\mathrm{t}}, \eta] = \Phi[\boldsymbol{\varphi}, \bar{\boldsymbol{e}}^{\mathrm{t}}, \eta] + \Omega[\boldsymbol{\varphi}], \qquad \Phi[\boldsymbol{\varphi}, \bar{\boldsymbol{e}}^{\mathrm{t}}, \eta] = \int_B \phi(\nabla\boldsymbol{\varphi}, \bar{\boldsymbol{e}}^{\mathrm{t}}, \eta, \nabla\eta)\mathrm{d}V, \tag{4}$$

where B denotes the body domain in the reference configuration, Φ represents the global Helmholtz free energy, and Ω represents the potential of the external loads, which in the case of the nominal surface traction $\boldsymbol{t}^*$ prescribed on the boundary ∂B_t is expressed as $\Omega[\boldsymbol{\varphi}] = -\int_{\partial B_t} \boldsymbol{t}^* \cdot \boldsymbol{\varphi}\,\mathrm{d}S$.

The rate-independent dissipation potential is adopted (in the incremental form) as

$$\Delta D(\Delta\eta) = f_{\mathrm{c}}|\Delta\eta|, \qquad \Delta\eta = \eta - \eta_n, \tag{5}$$

where $f_{\mathrm{c}} > 0$ is a material parameter (characterizing the width of the hysteresis loop in the intrinsic stress–strain response) and η_n is the volume fraction of martensite at the end of the previous step. Here and in the remainder of this paper, the subscript $n+1$ indicating the quantities at the current time step t_{n+1} is omitted for brevity.

Finally, the incremental solution in terms of the fields of $\boldsymbol{\varphi}$, $\bar{\boldsymbol{e}}^{\mathrm{t}}$ and η at instant t_{n+1} is obtained by minimizing the global incremental potential Π,

$$\{\boldsymbol{\varphi}, \bar{\boldsymbol{e}}^{\mathrm{t}}, \eta\} = \arg\min_{\boldsymbol{\varphi}, \bar{\boldsymbol{e}}^{\mathrm{t}}, \eta} \Pi[\boldsymbol{\varphi}, \bar{\boldsymbol{e}}^{\mathrm{t}}, \eta], \tag{6}$$

where Π is defined as

$$\Pi[\boldsymbol{\varphi}, \bar{\boldsymbol{e}}^{\mathrm{t}}, \eta] = \mathcal{E}[\boldsymbol{\varphi}, \bar{\boldsymbol{e}}^{\mathrm{t}}, \eta] - \mathcal{E}[\boldsymbol{\varphi}_n, \bar{\boldsymbol{e}}^{\mathrm{t}}_n, \eta_n] + \Delta\mathcal{D}[\eta] + \mathcal{I}_{[0,1]}[\eta] + \mathcal{I}_{\bar{\mathcal{P}}}[\bar{\boldsymbol{e}}^{\mathrm{t}}]. \tag{7}$$

The global dissipation potential $\Delta\mathcal{D}$ and the functionals $\mathcal{I}_{[0,1]}$ and $\mathcal{I}_{\bar{\mathcal{P}}}$ are defined as

$$\Delta\mathcal{D}[\eta] = \int_B \Delta D(\Delta\eta)\mathrm{d}V, \qquad \mathcal{I}_{[0,1]}[\eta] = \int_B I_{[0,1]}(\eta)\mathrm{d}V \qquad \mathcal{I}_{\bar{\mathcal{P}}}[\bar{\boldsymbol{e}}^{\mathrm{t}}] = \int_B I_{\bar{\mathcal{P}}}(\bar{\boldsymbol{e}}^{\mathrm{t}})\mathrm{d}V, \tag{8}$$

where $\mathcal{I}_{[0,1]}$ and $\mathcal{I}_{\bar{\mathcal{P}}}$ enforce, respectively, the physical constraint on the volume fraction of martensite, $0 \leq \eta \leq 1$, and the constraint on the limit transformation strain, $g(\bar{\boldsymbol{e}}^{\mathrm{t}}) = 0$, through the indicator functions,

$$I_{[0,1]}(\eta) = \begin{cases} 0 & \text{if } 0 \leq \eta \leq 1, \\ +\infty & \text{otherwise.} \end{cases} \qquad I_{\bar{\mathcal{P}}}(\bar{\boldsymbol{e}}^{\mathrm{t}}) = \begin{cases} 0 & \text{if } \bar{\boldsymbol{e}}^{\mathrm{t}} \in \bar{\mathcal{P}}, \\ +\infty & \text{otherwise.} \end{cases} \tag{9}$$

The treatment of the non-smooth dissipation $\Delta D(\Delta\eta)$ and the enforcement of the constraints $0 \leq \eta \leq 1$ and $g(\bar{\boldsymbol{e}}^{\mathrm{t}}) = 0$ are discussed in Section 3.3.

2.3. Specification of the components of the free energy ϕ

The individual components of the Helmholtz free energy ϕ in Eq. (3) are adopted as follows (see Stupkiewicz and Petryk, 2013; Rezaee-Hajidehi et al., 2020).

The chemical energy ϕ_0 is taken as the weighted average of the free energy densities of pure austenite and pure martensite phases, respectively, ϕ_0^{a} and ϕ_0^{m}, both in the stress-free state, i.e.

$$\phi_0(\eta) = (1-\eta)\phi_0^{\mathrm{a}} + \eta\phi_0^{\mathrm{m}} = \phi_0^{\mathrm{a}} + \Delta\phi_0\eta, \qquad \Delta\phi_0 = \phi_0^{\mathrm{m}} - \phi_0^{\mathrm{a}}, \tag{10}$$

where $\Delta\phi_0$ is known as the chemical energy of transformation. The dependence of $\Delta\phi_0$ on temperature is not explicitly indicated here, see Section 3.2 for the thermomechanically coupled model.

The (isotropic) elastic strain energy ϕ_{el} is adopted as

$$\phi_{\mathrm{el}}(\boldsymbol{F}, \bar{\boldsymbol{e}}^{\mathrm{t}}, \eta) = \frac{1}{2}\mu(\eta)(\operatorname{tr}\hat{\boldsymbol{b}}^{\mathrm{e}} - 3) + \frac{1}{4}\kappa(\det\boldsymbol{b}^{\mathrm{e}} - 1 - \log(\det\boldsymbol{b}^{\mathrm{e}})), \qquad \boldsymbol{b}^{\mathrm{e}} = \boldsymbol{F}\exp(-2\eta\bar{\boldsymbol{e}}^{\mathrm{t}})\boldsymbol{F}^{\mathrm{T}}, \tag{11}$$

where $\hat{\boldsymbol{b}}^{\mathrm{e}} = (\det\boldsymbol{b}^{\mathrm{e}})^{-1/3}\boldsymbol{b}^{\mathrm{e}}$ is the isochoric part of the elastic left Cauchy–Green tensor $\boldsymbol{b}^{\mathrm{e}} = \boldsymbol{F}^{\mathrm{e}}(\boldsymbol{F}^{\mathrm{e}})^{\mathrm{T}} = \boldsymbol{F}(\boldsymbol{C}^{\mathrm{t}})^{-1}\boldsymbol{F}^{\mathrm{T}}$, and $\boldsymbol{C}^{\mathrm{t}} = (\boldsymbol{F}^{\mathrm{t}})^{\mathrm{T}}\boldsymbol{F}^{\mathrm{t}} = \exp(2\eta\bar{\boldsymbol{e}}^{\mathrm{t}})$ in view of Eqs. (1) and (2). Using the Voigt mixing rule, the shear modulus $\mu(\eta) = (1-\eta)\mu_{\mathrm{a}} + \eta\mu_{\mathrm{m}}$ is obtained so that distinct shear moduli of austenite and martensite phases, respectively, μ_{a} and μ_{m}, are accounted for, while the bulk modulus κ is assumed constant during the phase transformation.

The interaction energy ϕ_{int} is adopted as

$$\phi_{\mathrm{int}}(\bar{\boldsymbol{e}}^{\mathrm{t}}, \eta) = \frac{1}{2}H(\bar{\boldsymbol{e}}^{\mathrm{t}})\eta^2, \tag{12}$$

where the interaction coefficient H determines the type of response during transformation (hardening- or softening-like depending on the sign of H) and is assumed to be a function of the transformation strain $\bar{\boldsymbol{e}}^{\mathrm{t}}$. The explicit form of the interaction coefficient H is introduced and discussed in Section 2.5.

Finally, the gradient energy component ϕ_{grad} takes the form

$$\phi_{\mathrm{grad}}(\nabla\eta) = \frac{1}{2} G \nabla\eta \cdot \nabla\eta, \tag{13}$$

where the operator ∇ denotes the gradient with respect to the reference configuration and parameter $G > 0$ characterizes the energy associated with the gradient of η. According to the analytical solution of the one-dimensional small-strain version of the model, for a softening-like response resulting from a negative constant interaction coefficient $H < 0$, a characteristic length, which represents the theoretical thickness of the diffuse austenite–martensite interface, is obtained as $\lambda = \pi\sqrt{-G/H}$ (Rezaee-Hajidehi and Stupkiewicz, 2018). Since H is defined here as a function of the transformation strain $\bar{\boldsymbol{e}}^{\mathrm{t}}$, see Eq. (17), the interface thickness is not constant and depends on $\bar{\boldsymbol{e}}^{\mathrm{t}}$.

2.4. The surface of limit transformation strains, $g(\bar{\boldsymbol{e}}^{t}) = 0$

The function g is inherited, with a small modification, from the model of Sadjadpour and Bhattacharya (2007) and is capable of describing tension–compression asymmetry and transverse isotropy. These properties are indeed of great importance for the particular study aimed in this paper. The function g is expressed as

$$g(\bar{\boldsymbol{e}}^{\mathrm{t}}) = \Big[(-I_2)^{3/2} - bI_3 - cI_4^3\Big]^{1/3} - a \tag{14}$$

where I_k are the invariants of the transformation strain tensor $\bar{\boldsymbol{e}}^{\mathrm{t}}$ and are expressed as

$$I_2 = -\frac{1}{2}\operatorname{tr}(\bar{\boldsymbol{e}}^{\mathrm{t}})^2, \qquad I_3 = \det \bar{\boldsymbol{e}}^{\mathrm{t}}, \qquad I_4 = \boldsymbol{m} \cdot \bar{\boldsymbol{e}}^{\mathrm{t}} \boldsymbol{m}, \tag{15}$$

with $\boldsymbol{m}$ as the axis of the transverse isotropy. The parameters a, b and c in Eq. (14) read

$$a = \epsilon_{\mathrm{T}}\Big[\frac{3\sqrt{3}}{4(1+\alpha^3)}\Big]^{1/3}, \qquad b = \frac{\sqrt{3}}{6}\frac{9\alpha^3\beta^3 - 7\alpha^3 + 7\beta^3 - 9}{(1+\alpha^3)(1+\beta^3)}, \qquad c = \frac{2\sqrt{3}}{3}\frac{\alpha^3 - \beta^3}{(1+\alpha^3)(1+\beta^3)}, \tag{16}$$

where $\alpha = \epsilon_{\mathrm{T}}/\epsilon_{\mathrm{C}}$ is the ratio between the maximum tensile and compressive transformation strains in the direction along $\boldsymbol{m}$ and $\beta = \epsilon^*_{\mathrm{T}}/\epsilon^*_{\mathrm{C}}$ is the ratio between the maximum tensile and compressive transformation strains in the direction perpendicular to $\boldsymbol{m}$. Note that an isotropic material with and without tension–compression asymmetry is described by $\alpha = \beta \neq 1$ and $\alpha = \beta = 1$, respectively, whereas $\alpha \neq \beta$ corresponds to transverse isotropy.

To illustrate the surface of limit transformation strains generated by $g(\bar{\boldsymbol{e}}^{\mathrm{t}}) = 0$ and the associated dual surface of transformation-onset stresses (jointly referred to as 'transformation surfaces' in the

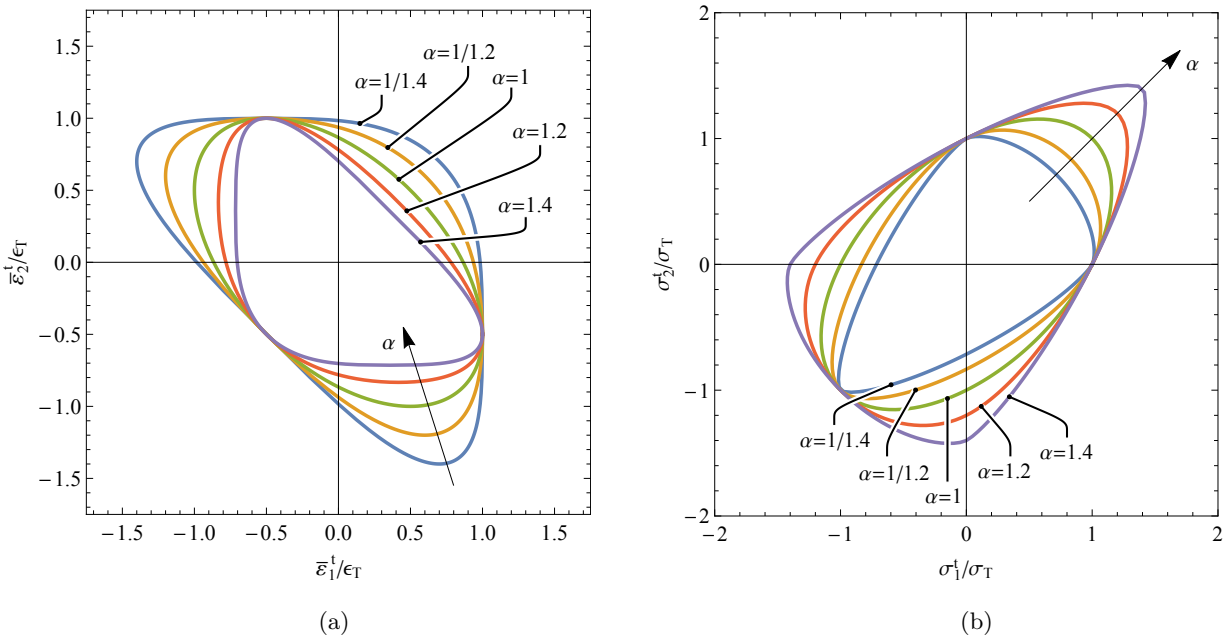

Figure 1: The effect of parameter α on (a) the surface of limit transformation strains and (b) the surface of transformation-onset stresses of an isotropic material ($\beta = \alpha$) in the biaxial stress state.

sequel), the effect of parameters α and β on the shape of the respective surfaces in a material subjected to biaxial stress state and combined tension–shear is examined. The biaxial stress state has been chosen for this illustration because the corresponding transformation surfaces clearly reflect the effect of parameters α and β, while, combined tension–shear is related to the main simulations presented in Section 4.

The transformation surfaces are determined at the material-point level. Thus, the gradient energy term ϕ_{grad} in the Helmholtz free energy function, see Eq. (3), is disregarded here. Additionally, in order to simplify the numerical procedure, the small-strain version of the model is employed for this specific purpose, check Appendix A for the related procedure.

Figure 1 depicts the effect of parameter α on the transformation surfaces of an isotropic material ($\beta = \alpha$) subjected to a biaxial stress state. In Fig. 1 and in the subsequent figures in this section, the limit transformation strains $\bar{\varepsilon}_1^t$ and $\bar{\varepsilon}_2^t$ ($\bar{\varepsilon}^t$ and $\bar{\gamma}^t$ in the case of combined tension–shear), where $\bar{\boldsymbol{\varepsilon}}^t$ is the small-strain counterpart of $\bar{\boldsymbol{\varepsilon}}^t$, and the transformation-onset stresses σ_1^t and σ_2^t (σ^t and τ^t in the case of combined tension–shear) are normalized, respectively, by the maximum transformation strain ϵ_T and the transformation-onset stress σ_T in uniaxial tension. Recall that the case of $\alpha = \beta = 1$ corresponds to an isotropic material without tension–compression asymmetry, and the corresponding transformation-onset stress surface, see the respective surface in Fig. 1(b), forms an ellipse, retrieving the von Mises yield surface. Note that, on account of isotropy, the transformation surfaces are symmetric about the respective lines $\bar{\varepsilon}_1^t = \bar{\varepsilon}_2^t$ and $\sigma_1^t = \sigma_2^t$.

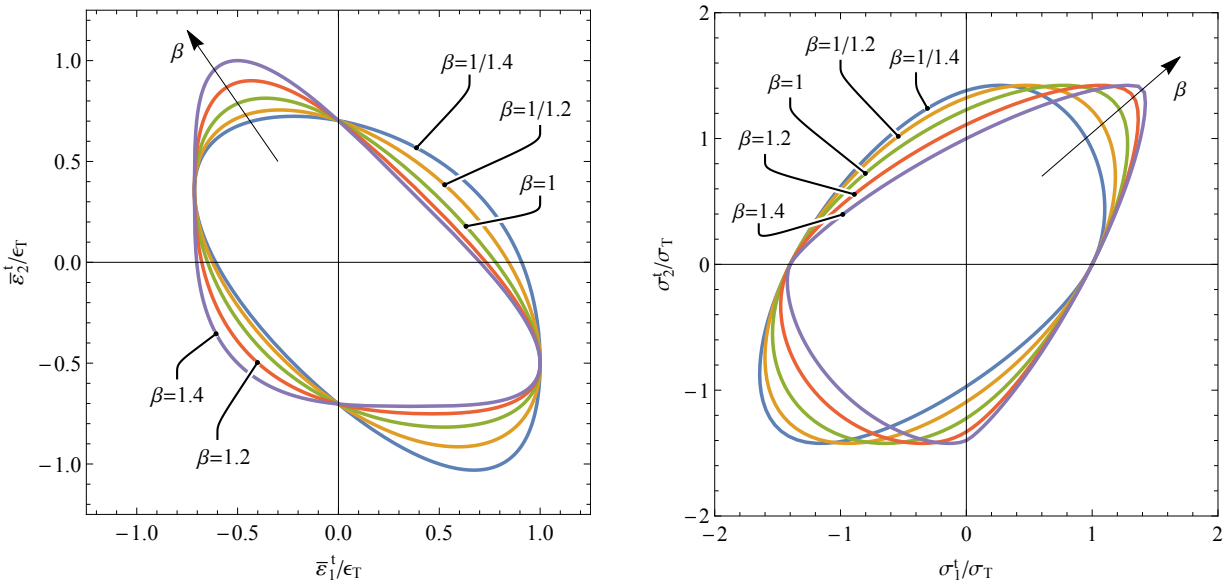

Figure 2: The effect of parameter β on (a) the surface of limit transformation strains and (b) the surface of transformation-onset stresses of a transversely isotropic material ($\boldsymbol{m} = \boldsymbol{i}_1$) in the biaxial stress state. The parameter $\alpha = 1.4$ is fixed.

The effect of parameter β on the transformation surfaces of a material subjected to a biaxial stress state is shown in Fig. 2. Parameter $\alpha = 1.4$ is here fixed and the axis of transverse isotropy $\boldsymbol{m}$ is oriented along the direction $\boldsymbol{i}_1 = (1, 0, 0)$, thus $\boldsymbol{m} = \boldsymbol{i}_1$. It can be seen that, as β deviates from α, the transformation surfaces lose their symmetry. Since the axis of transverse isotropy $\boldsymbol{m}$ is directed along $\boldsymbol{i}_1$, the transformation-onset stress σ_1^{t} is not affected by the change of β in the case of uniaxial tension or compression along $\boldsymbol{i}_1$, see the line $\sigma_2^{\mathrm{t}} = 0$. On the other hand, in the case of uniaxial tension or compression along $\boldsymbol{i}_2 = (0, 1, 0)$, the transformation-onset stress σ_2^{t} varies as a function of β, see the line $\sigma_1^{\mathrm{t}} = 0$.

Next, as a preliminary study towards the main simulations presented in Section 4, the effect of parameters α and β on the transformation surfaces of a material subjected to combined tension–shear is illustrated in Figs. 3 and 4. The transformation surfaces in this case are represented by $\bar{\varepsilon}^{\mathrm{t}}$–$\bar{\gamma}^{\mathrm{t}}$ and σ^{t}–τ^{t} sections, where $(\bar{\varepsilon}^{\mathrm{t}}, \sigma^{\mathrm{t}})$ and $(\bar{\gamma}^{\mathrm{t}}, \tau^{\mathrm{t}})$ are the respective axial and shear components. Due to the symmetry of the transformation surfaces about the respective axes $\bar{\gamma}^{\mathrm{t}} = 0$ and $\tau^{\mathrm{t}} = 0$, only the upper half of each surface is shown. Note that, for the transversely isotropic case, $\beta \neq \alpha$, in Fig. 4, the axis of transverse isotropy $\boldsymbol{m}$ is directed along the axis of tension.

The discussion of the results given in Figs. 3 and 4 is deferred to Section 2.5. It will be shown that upon defining a suitable interaction coefficient H and taking the advantage of the tension–compression asymmetry and transverse isotropy properties of the function g (characterized

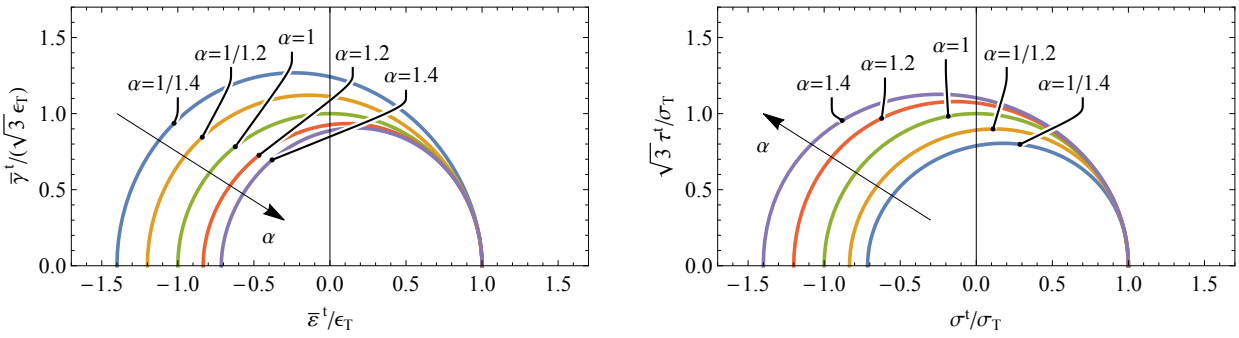

(a) (b)

Figure 3: The effect of parameter α on (a) the surface of limit transformation strains and (b) the surface of transformation-onset stresses of an isotropic material ($\beta = \alpha$) under combined tension–shear loading.

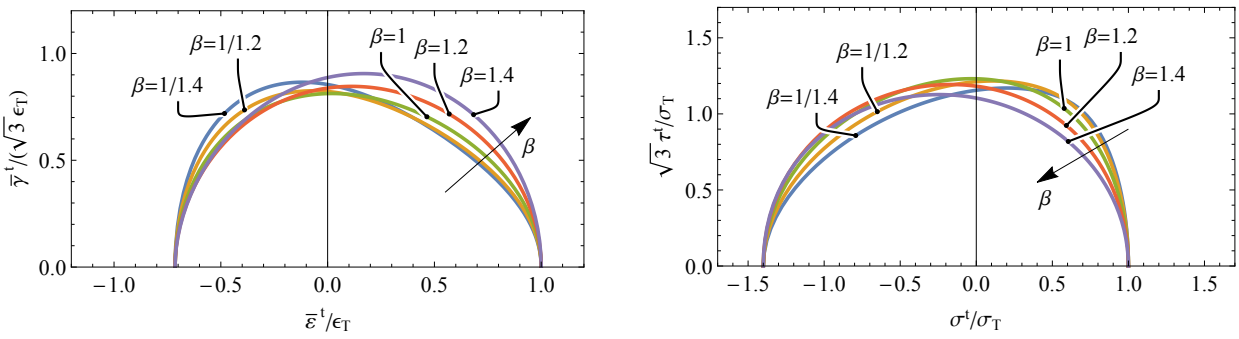

(a) (b)

Figure 4: The effect of parameter β on (a) the surface of limit transformation strains and (b) the surface of transformation-onset stresses of a transversely isotropic material under combined tension–shear loading. The parameter $\alpha = 1.4$ is fixed, and $\boldsymbol{m}$ is directed along the axis of tension.

by parameters α and β), a softening-like material response under uniaxial tension and a hardening-like response under shear can be obtained.

2.5. The interaction coefficient $H(\bar{\boldsymbol{e}}^t)$

The tension–compression asymmetry is a well-known characteristic of NiTi that has been commonly observed in experiments. In particular, NiTi exhibits higher transformation stress and lower transformation strain under compression with respect to those under tension. The tension–compression asymmetry also applies to the type of the material response in terms of hardening/softening during transformation. Typically, softening is observed in tension, while hardening in compression (e.g. Bechle and Kyriakides, 2014; Reedlunn et al., 2014, 2020a). Note that this type of tension–compression asymmetry is not a common feature in phenomenological models of pseudoelasticity (e.g., Jiang et al., 2017a,b,c; Rezaee-Hajidehi et al., 2020; Frost et al., 2020).

The response of NiTi in shear has also been examined in a number of experimental works (see e.g. Orgéas and Favier, 1998; Sun and Li, 2002; Grabe and Bruhns, 2009; Reedlunn et al., 2020a). The main consensus is that the shear response is characterized by a hardening-like behaviour. Besides, the transformation stress in shear, when expressed in terms of the equivalent stress, lies between the transformation stresses in tension and in compression.

According to the above experimental observations, the interaction coefficient H, which characterizes the material response in the transformation regime, is proposed to depend on the transformation strain $\bar{\boldsymbol{e}}^{\mathrm{t}}$, and the following constitutive function is adopted for that purpose (Rezaee-Hajidehi et al., 2020),

$$H(\bar{\boldsymbol{e}}^{\mathrm{t}}) = H_{\mathrm{T}} - \frac{(\epsilon_{\mathrm{T}} - \epsilon(\bar{\boldsymbol{e}}^{\mathrm{t}}))(H_{\mathrm{T}} - H_{\mathrm{C}})}{\epsilon_{\mathrm{T}} - \epsilon_{\mathrm{C}}}, \qquad \epsilon(\bar{\boldsymbol{e}}^{\mathrm{t}}) = \sqrt{\frac{2}{3}\,\mathrm{tr}(\bar{\boldsymbol{e}}^{\mathrm{t}})^2}, \tag{17}$$

where $\epsilon(\bar{\boldsymbol{e}}^{\mathrm{t}})$ is the equivalent transformation strain, H_{T} and H_{C} represent, respectively, the hardening modulus (softening is obtained for $H_{\mathrm{T}} < 0$) associated with the uniaxial tension (when $\epsilon(\bar{\boldsymbol{e}}^{\mathrm{t}}) = \epsilon_{\mathrm{T}}$) and the hardening modulus associated with the uniaxial compression (when $\epsilon(\bar{\boldsymbol{e}}^{\mathrm{t}}) = \epsilon_{\mathrm{C}}$). Recall that, according to the definition of function $g(\bar{\boldsymbol{e}}^{\mathrm{t}})$ in Eqs. (14)–(16), parameters ϵ_{T} and ϵ_{C} correspond to the uniaxial tension and compression along the axis $\boldsymbol{m}$ of transverse isotropy, and so do the hardening moduli H_{T} and H_{C}. The response in shear is expected to be intermediate between the uniaxial tension and compression. However, as shown below, the actual behaviour in shear is significantly affected by transverse isotropy.

A material-point study has been performed to investigate the effect of transverse isotropy, as described by parameter β, on the pseudoelastic response under uniaxial tension, shear and uniaxial compression. As in Section 2.4, the contribution of the gradient energy term ϕ_{grad} to the Helmholtz free energy is disregarded, since the intrinsic material response refers to a homogeneous deformation. The analysis is performed in the finite-strain setting. The material is subjected to a mixed-control

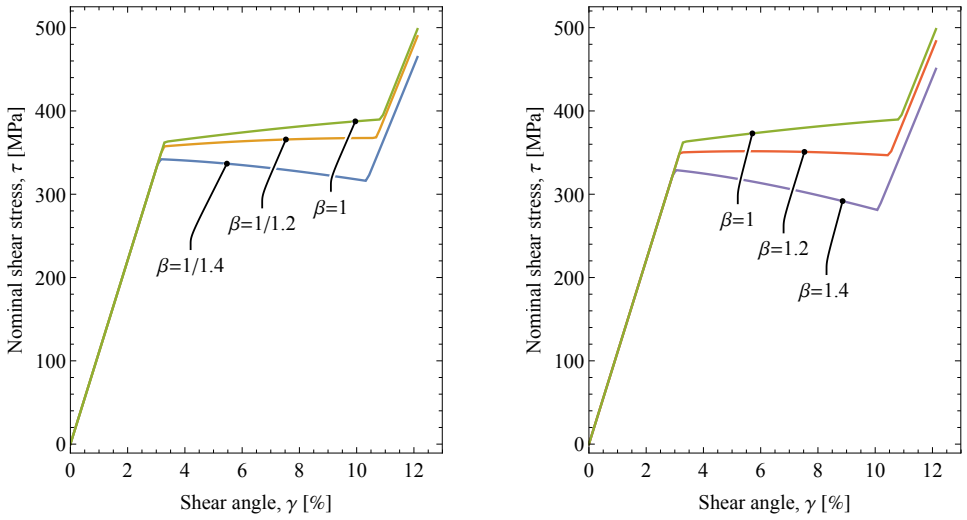

Figure 5: The effect of parameter β on the nominal shear stress–shear angle response of NiTi under shear during loading: (a) $\beta \leq 1$ and (b) $\beta \geq 1$. The parameter $\alpha = 1.4$ is fixed.

loading that corresponds to the loading of a tubular specimen, cf. Section 4. Specifically, the engineering axial strain ε and shear angle γ are here prescribed, and the resulting nominal axial stress σ and shear stress τ are determined. At the same time, all the remaining components of the (Cauchy) stress tensor are enforced to be equal to zero. The hardening moduli are adopted as $H_{\mathrm{T}} = -5$ MPa and $H_{\mathrm{C}} = 7$ MPa. With the exception of parameter $\alpha = 1.4$ and β that varies between $1/\alpha$ and α, the other material parameters are taken as those in the study in Section 4. The axis of transverse isotropy $\boldsymbol{m}$ is directed along the axis of tension.

Figure 5 shows the effect of parameter β on the nominal shear stress–shear angle response under shear (null axial strain, $\varepsilon = 0$) during loading. It can be seen that parameter β not only changes the transformation-onset stress in shear (see also Fig. 4), but also has a significant impact on the response in the transformation branch. In particular, the maximum level of hardening is achieved when β is equal to unity. On the other hand, as β diverges from unity, the level of associated hardening decreases.

To further investigate the effect of β on the pseudoelastic response, two representative values of β are chosen, namely $\beta = \alpha = 1.4$ and $\beta = 1$, and for each value, the response under uniaxial tension, shear and uniaxial compression is plotted in Fig. 6. The plots show the corresponding equivalent stress–equivalent strain curves, where the equivalent stress σ_{eq} and the equivalent strain $\varepsilon_{\mathrm{eq}}$ are defined as

$$\sigma_{\mathrm{eq}} = \sqrt{\sigma^2 + 3\tau^2}, \qquad \varepsilon_{\mathrm{eq}} = \sqrt{\varepsilon^2 + \gamma^2/3}. \tag{18}$$

It follows that parameter β does not affect the response in uniaxial tension and uniaxial compres-

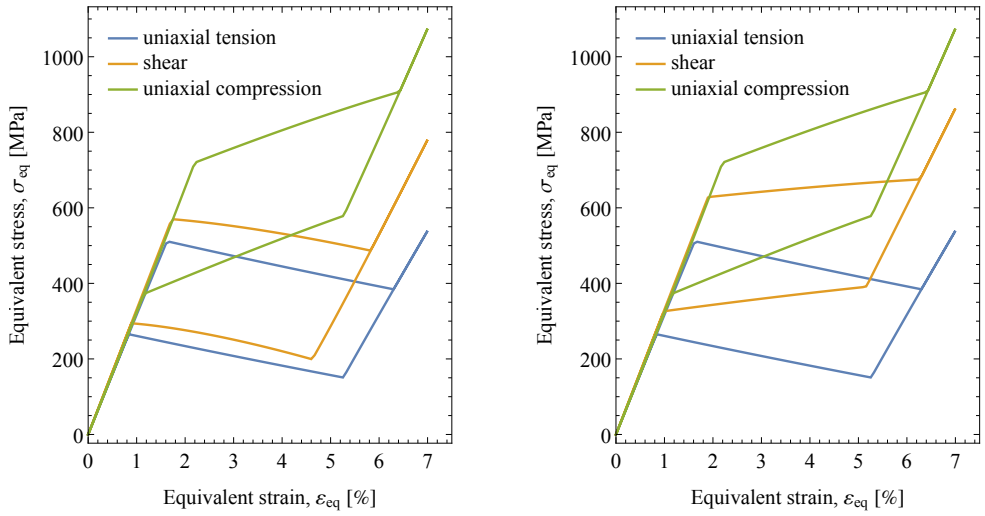

(a) (b)

Figure 6: The effect of parameter β on the equivalent stress–equivalent strain response of NiTi under uniaxial tension, shear and uniaxial compression: (a) $\beta = \alpha = 1.4$ and (b) $\beta = 1$ and $\alpha = 1.4$. Note that only the response in shear is affected by β.

sion, see also Fig. 4. The response in shear, regardless of the value of parameter β, always remains intermediate between the uniaxial tension and compression responses. For $\beta = \alpha = 1.4$, although the transformation-onset stress in shear is slightly higher than that of uniaxial tension, the corresponding levels of softening are almost the same. On the other hand, for $\beta = 1$, a hardening-like response is obtained in shear, as already shown in Fig. 5. This shows that it is crucial to account for the transverse isotropy of the transformation strain ($\beta \neq \alpha$) to be able to simultaneously describe a softening-like response in tension and a hardening-like response in shear, and the effect is maximized when $\beta = 1$.

Remark 1. The combination of parameters such that α is larger than unity and β is smaller than α and, say, close to unity, as discussed above, is actually physically relevant. In fact, NiTi tubes (as well as wires and rods) typically exhibit the drawing texture in which the $\langle 111 \rangle$ poles of the austenite are preferably aligned with the tube axis. For such a texture, the tensile transformation strain is the highest for the loading along the tube axis, and this is accompanied by a significant tension–compression asymmetry along this direction (e.g. Thamburaja and Anand, 2001).

Remark 2. The stress–strain response predicted by the present model is approximately trilinear with an abrupt change of the slope at the onset and saturation of the transformation. The actual material response is smooth (e.g. Lim and McDowell, 1999; Grabe and Bruhns, 2008; Wang et al., 2010), as can be predicted by the micromechanical models (e.g. Thamburaja and Anand, 2001; Stupkiewicz and Petryk, 2010). The non-monotonic material response revealed by Hallai and Kyriakides (2013)

is smooth as well, and such a non-monotonic response is predicted by a micromechanical model in which the interfacial energy contributions are accounted for at several relevant spatial scales (Stupkiewicz et al., 2020).

3. Finite-element implementation

3.1. The micromorphic regularization

The finite-element implementation of the gradient-enhanced model presented in Section 2.2 is not convenient due to the presence of the Laplacian of the volume fraction η in the transformation criterion. Accordingly, a micromorphic-type regularization is employed as a tool to facilitate the finite-element implementation of the model. Details can be found in Rezaee-Hajidehi and Stupkiewicz (2018) and Rezaee-Hajidehi et al. (2020), see also Mazière and Forest (2015), as well as Forest (2009) for a general context.

To perform the micromorphic regularization of the gradient-enhanced model, the gradient energy term ϕ_{grad} in the Helmholtz free energy function, Eq. (3), is replaced by its micromorphic counterpart,

$$\phi_{\mathrm{grad}}(\eta, \breve{\eta}, \nabla\breve{\eta}) = \frac{1}{2} G \nabla\breve{\eta} \cdot \nabla\breve{\eta} + \frac{1}{2}\chi(\eta - \breve{\eta})^2, \tag{19}$$

where a new variable $\breve{\eta}$, the micromorphic counterpart of η, as well as a new regularization parameter χ, which penalizes the discrepancy between η and $\breve{\eta}$, have been introduced. As a result of this substitution, the Helmholtz free energy function takes the form

$$\phi(\boldsymbol{F}, \bar{\boldsymbol{e}}^{\mathrm{t}}, \eta, \breve{\eta}, \nabla\breve{\eta}) = \phi_0(\eta) + \phi_{\mathrm{el}}(\boldsymbol{F}, \bar{\boldsymbol{e}}^{\mathrm{t}}, \eta) + \phi_{\mathrm{int}}(\bar{\boldsymbol{e}}^{\mathrm{t}}, \eta) + \phi_{\mathrm{grad}}(\eta, \breve{\eta}, \nabla\breve{\eta}). \tag{20}$$

Consequently, the evolution problem (6) is replaced by the global minimization problem with respect to the fields of $\boldsymbol{\varphi}$, $\bar{\boldsymbol{e}}^{\mathrm{t}}$, η and $\breve{\eta}$,

$$\{\boldsymbol{\varphi}, \bar{\boldsymbol{e}}^{\mathrm{t}}, \eta, \breve{\eta}\} = \arg \min_{\boldsymbol{\varphi}, \bar{\boldsymbol{e}}^{\mathrm{t}}, \eta, \breve{\eta}} \Pi[\boldsymbol{\varphi}, \bar{\boldsymbol{e}}^{\mathrm{t}}, \eta, \breve{\eta}], \tag{21}$$

where the global incremental potential Π is formulated, in analogy to Eq. (7), in terms of the global potential energy $\mathcal{E}$ defined as

$$\mathcal{E}[\boldsymbol{\varphi}, \bar{\boldsymbol{e}}^{\mathrm{t}}, \eta, \breve{\eta}] = \Phi[\boldsymbol{\varphi}, \bar{\boldsymbol{e}}^{\mathrm{t}}, \eta, \breve{\eta}] + \Omega[\boldsymbol{\varphi}], \qquad \Phi[\boldsymbol{\varphi}, \bar{\boldsymbol{e}}^{\mathrm{t}}, \eta, \breve{\eta}] = \int_B \phi(\nabla\boldsymbol{\varphi}, \bar{\boldsymbol{e}}^{\mathrm{t}}, \eta, \breve{\eta}, \nabla\breve{\eta}) \mathrm{d}V. \tag{22}$$

The beneficial feature of the micromorphic formulation is that the minimization with respect to η can be performed pointwise (i.e. locally at each integration point), which leads to a straightforward finite-element implementation (Rezaee-Hajidehi and Stupkiewicz, 2018; Rezaee-Hajidehi et al., 2020).

3.2. The thermomechanically coupled model

Although the finite-element simulations in this study, Section 4, are carried out in nearly isothermal conditions (thus almost no temperature gradient exists), a thermomechanically coupled model is employed in the computations. Following Rezaee-Hajidehi et al. (2020), the thermomechanical couplings are included in the model through the temperature dependence of the chemical energy ϕ_0 in the Helmholtz free energy function, Eq. (3), and through the internal heat source associated with the phase transformation. These two essential couplings are briefly described below, while a general case including all related couplings is described in Appendix B in Rezaee-Hajidehi et al. (2020).

First, the chemical energy in Eq. (10) is reformulated in terms of volume fraction η and temperature T as,

$$\phi_0(\eta, T) = \phi_0^{\mathrm{a}}(T) + \Delta\phi_0(T)\eta, \qquad \Delta\phi_0(T) = \Delta s^*(T - T_{\mathrm{t}}), \tag{23}$$

where Δs^* is the entropy difference between the pure austenite and pure martensite phases and T_{t} is the equilibrium temperature. Note that the form $(23)_2$ for the chemical energy of transformation, $\Delta\phi_0$, is obtained thanks to the assumption of identical specific heat capacities for pure austenite and pure martensite phases, $c^{\mathrm{a}} = c^{\mathrm{m}} = c$.

Next, the internal heat source $\dot{R}$ is expressed as

$$\dot{R} = \Delta s^* T\dot{\eta} + f_{\mathrm{c}}|\dot{\eta}|, \tag{24}$$

where the overdot denotes the derivative with respect to time. The first and second terms in Eq. (24) represent, respectively, the latent heat of transformation and the heat due to mechanical dissipation.

Finally, the heat conduction equation (in the reference configuration) is written as

$$\varrho_0 c\dot{T} + \nabla \cdot \boldsymbol{Q} = \dot{R}, \qquad \boldsymbol{Q} = -K\boldsymbol{C}^{-1}\nabla T, \tag{25}$$

where $\varrho_0 c$ is the specific heat, $\boldsymbol{Q}$ is the nominal heat flux, $\boldsymbol{C} = \boldsymbol{F}^{\mathrm{T}}\boldsymbol{F}$ is the right Cauchy–Green tensor and K is the heat conductivity coefficient. See, e.g., Holzapfel (2006) for more details.

3.3. Finite-element treatment

The finite-element treatment of the model follows that applied by Rezaee-Hajidehi et al. (2020), where all the details can be found. The complete thermomechanical problem, consisting of the global minimization problem (21) for the mechanical part and the heat conduction equation (25) for the thermal part, comprises five unknown fields, out of which $\boldsymbol{u} = \boldsymbol{\varphi} - \boldsymbol{X}$, $\breve{\eta}$ and T are global unknowns, while η and $\bar{\boldsymbol{e}}^{\mathrm{t}}$ are local variables. In the finite-element implementation of the model, the quadratic serendipity hexahedral (20-noded) element with a reduced (2×2×2) integration rule is

employed for the displacement field $\boldsymbol{u}$, while the tri-linear hexahedral (8-noded) element is employed for the fields of $\breve{\eta}$ and T. The serendipity element proved to be computationally more efficient than the tri-quadratic (27-noded) hexahedral element used in our previous study (Rezaee-Hajidehi et al., 2020).

In analogy to the global minimization problem (21), the local (point-wise) minimization with respect to η and $\bar{\boldsymbol{e}}^{\mathrm{t}}$ is formulated as

$$\{\bar{\boldsymbol{e}}^{\mathrm{t}}, \eta\} = \arg\min_{\bar{\boldsymbol{e}}^{\mathrm{t}}, \eta} \pi(\boldsymbol{F}, \bar{\boldsymbol{e}}^{\mathrm{t}}, \eta, \breve{\eta}, \nabla\breve{\eta}), \tag{26}$$

where $\boldsymbol{F}$, $\breve{\eta}$ and $\nabla\breve{\eta}$ are considered to be known, and the local potential π takes the form,

$$\pi(\boldsymbol{F}, \bar{\boldsymbol{e}}^{\mathrm{t}}, \eta, \breve{\eta}, \nabla\breve{\eta}) = \phi(\boldsymbol{F}, \bar{\boldsymbol{e}}^{\mathrm{t}}, \eta, \breve{\eta}, \nabla\breve{\eta}) - \phi(\boldsymbol{F}_n, \bar{\boldsymbol{e}}^{\mathrm{t}}_n, \eta_n, \breve{\eta}_n, \nabla\breve{\eta}_n) + \Delta D(\eta - \eta_n) + I_{[0,1]}(\eta) + I_{\bar{\mathcal{P}}}(\bar{\boldsymbol{e}}^{\mathrm{t}}). \tag{27}$$

Due to the presence of the non-differentiable term $\Delta D + I_{[0,1]}$, the local potential π is non-smooth in η. To treat this, the augmented Lagrangian technique (cf. Stupkiewicz and Petryk, 2013) has been exploited. On the other hand, the usual Lagrange multiplier technique has been used to address the equality constraint $g(\bar{\boldsymbol{e}}^{\mathrm{t}}) = 0$ that appears in the minimization of π with respect to $\bar{\boldsymbol{e}}^{\mathrm{t}}$ through the indicator function $I_{\bar{\mathcal{P}}}$. For details, see Rezaee-Hajidehi et al. (2020).

On the global level, the Newton method is used to solve (in a monolithic manner) the coupled nonlinear equations resulting from the finite-element discretization. Automatic differentiation technique has been employed using the *Mathematica* toolbox *AceGen* (Korelc, 2009; Korelc and Wriggers, 2016) to efficiently compute the derivatives involved in the finite-element procedure. As a result, due to the exact linearization of the nonlinear equations, the quadratic convergence of the Newton method is ensured. The finite-element code generated by *AceGen* is then implemented in the *Mathematica* toolbox *AceFEM* to perform the finite-element simulations. A direct solver (Intel MKL PARDISO) is used for solving the system of linear equations at each Newton iteration.

4. Analysis of a NiTi tube under combined tension–torsion

The main aim of the simulations presented in this section is to study formation and evolution of transformation patterns in a NiTi tube subjected to combined tension–torsion loading. For this purpose, the experiment of Sun and Li (2002), see also Li and Sun (2002), is considered as a reference for the geometry and characterization of the material parameters of the NiTi tube under study, cf. Section 4.1. In Section 4.2, the simulation results related to the NiTi tube under uniaxial tension are presented as a baseline for subsequent comparisons. The results of the simulations of combined tension–torsion are then discussed in Section 4.3. In Section 4.4, a detailed study is carried out regarding the transformation yield stress locus of NiTi under combined tension–torsion.

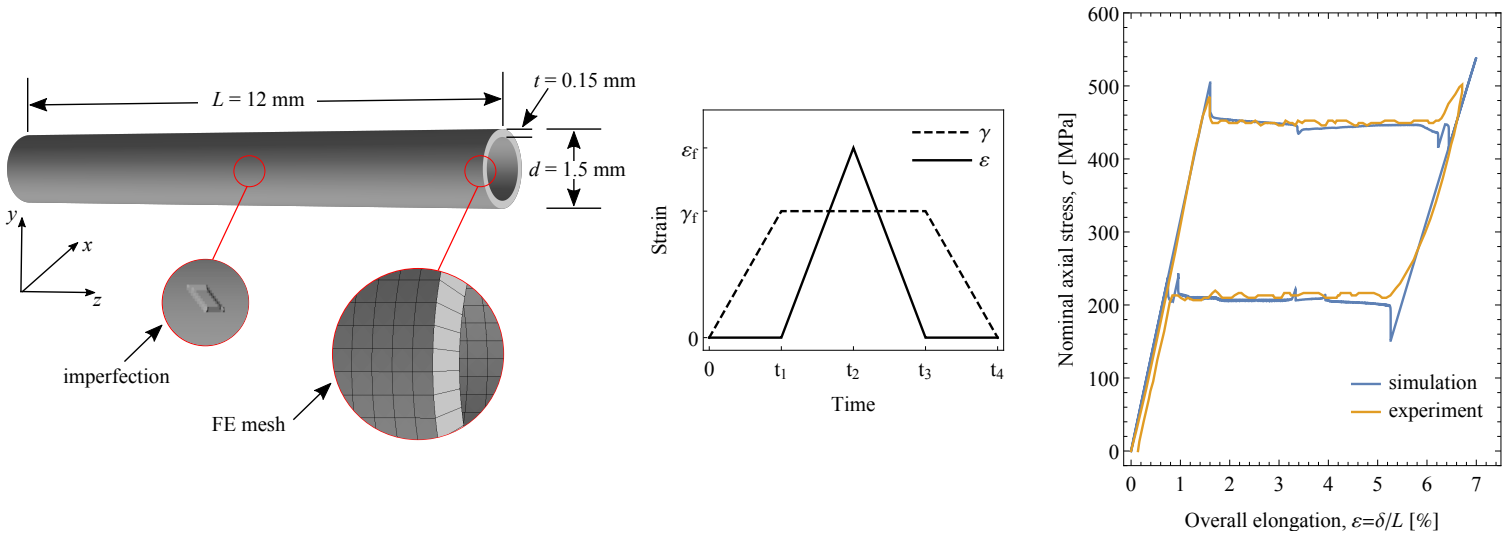

(a) (b) (c)

Figure 7: NiTi tube under combined tension–torsion: (a) the geometry of the tube, (b) the loading program and (c) the nominal axial stress–elongation response under uniaxial tension. The experimental curve in panel (c) refers to the results of Sun and Li (2002), which have been used to calibrate the model parameters.

4.1. Description of the problem

The geometry of the tube is depicted in Fig. 7(a). The outer diameter and the wall thickness of the tube are, respectively, $d = 1.5$ mm and $t = 0.15$ mm, as in the experiment (Sun and Li, 2002). To reduce the computational cost, the length of the tube is taken as $L = 12$ mm, which is about 4 times smaller than the one in the experiment (52 mm). It has been observed that employing a longer tube in the simulations does not lead to qualitatively different predictions. This is commented in Section 4.2.

Similar to the experiment, the ambient temperature is fixed to the room temperature $T_0 = 296$ K. The heat-sink effect of the grips in the experiment is mimicked by prescribing the temperature at both ends of the tube equal to the ambient temperature T_0. The simulations are carried out at a constant strain rate of $2 \times 10^{-5}\,1/\mathrm{s}$, which results in nearly isothermal conditions. The loading program is shown in Fig. 7(b). First, the tube is twisted by increasing the *overall* shear angle γ, while the *overall* elongation ε is kept at zero. After reaching the maximum overall shear angle $\gamma = \gamma_\mathrm{f}$, the overall elongation ε is increased until $\varepsilon = \varepsilon_\mathrm{f}$ is reached. The unloading proceeds in the reverse order.

The overall elongation $\varepsilon = \delta/L$ and the overall shear angle $\gamma = \phi\, d/(2L)$ are applied by prescribing, respectively, the axial displacement δ and the angle of twist ϕ at the nodes located at $Z_i = L$, where Z_i denotes the axial reference placement of the i-th node. At the same time, the axial displacement and rotation are constrained at $Z_i = 0$. Uniform radial expansion or contraction is allowed by

Table 1: Material parameters adopted in the computations.

κ	μ_a	μ_m	Δs^*	f_c	H_T	H_C	T_t	ϵ_T	α	β	$\varrho_0 c$	K	G	χ
[GPa]	[GPa]	[GPa]	[MPa/K]	[MPa]	[MPa]	[MPa]	[K]	[-]	[-]	[-]	[MJ/(m^3 K)]	[W/(m K)]	[Pa m^2]	[MPa]
130	11	8.5	0.24	6	-5	7	220	0.045	1.25	1	2.86	18	10^{-3}	500

applying the boundary condition $y_i X_i - x_i Y_i = 0$ at $Z_i = 0$ and $y_i X_i - x_i Y_i = (x_i X_i + y_i Y_i) \tan\phi$ at $Z_i = L$, where (X_i, Y_i) and (x_i, y_i) denote, respectively, the reference and current placement of the i-th node in the respective plane. Accordingly, the deformation is homogeneous in the entire tube until strain localization is triggered by an imperfection, as discussed below. Similar boundary conditions have been used, for instance, by Jiang et al. (2017b).

The material parameters are selected as follows. The bulk modulus $\kappa = 130$ GPa and the shear moduli $\mu_\mathrm{a} = 11$ GPa (for austenite) and $\mu_\mathrm{m} = 8.5$ GPa (for martensite) are adopted. The chemical energy of transformation $\Delta s^* = 0.24$ MPa/K is taken as in our previous studies (Rezaee-Hajidehi et al., 2020). The parameters $T_\mathrm{t} = 220$ K, $f_\mathrm{c} = 6$ MPa and $\epsilon_\mathrm{T} = 0.045$ are selected such that the stress at the onset of transformation, the transformation strain, and the width of the hysteresis loop in the uniaxial tensile response of the NiTi tube match approximately those in the experiment, see Fig. 7(c). Similarly, the hardening modulus $H_\mathrm{T} = -5$ MPa is determined in a way that the level of the stress plateau in the uniaxial tensile response is approximately the same as the one in the experiment. On the other hand, the hardening modulus $H_\mathrm{C} = 7$ MPa is adopted according to the homogeneous response of NiTi in compression (Bechle and Kyriakides, 2014; Reedlunn et al., 2014). The parameters characterizing the tension–compression asymmetry and transverse isotropy are adopted as $\alpha = 1.25$ and $\beta = 1$, with the axis of transverse isotropy $\boldsymbol{m}$ directed along the tube axis. The value of α is in the typical range for NiTi, while the value of β is selected based on the results of the parametric study presented in Section 2.5. The thermal parameters, i.e. $\varrho_0 c = 2.86$ MJ/(m^3 K) and $K = 18$ W/(m K), are taken as those in our previous studies (Rezaee-Hajidehi and Stupkiewicz, 2018; Rezaee-Hajidehi et al., 2020).

The two parameters related to the gradient enhancement are adopted as $G = 10^{-3}$ Pa m^2 and $\chi = 500$ MPa. The wall thickness is here relatively large ($d/t = 10$) so that the 3D effects provide a substantial regularization of the localization bands (Mazière and Forest, 2015; Rezaee-Hajidehi et al., 2020), and a small value of G is thus sufficient. Note, however, that the effect of the gradient enhancement, even if small, is still important, as it significantly improves robustness of the model. Preliminary studies have shown that, for a vanishingly small value of G, the computations were almost twice slower and the overall response exhibited spurious oscillations. The adopted value of parameter χ ensures that the discrepancy between the micromorphic variable $\breve{\eta}$ and the local volume fraction η is negligibly small. All model parameters are summarized in Table 1.

The finite-element size is fixed to 0.065 mm within the surface of the tube. The tube is thus discretized with 72 and 184 elements along the perimeter and height, respectively, and one element in the thickness direction. This results in the total number of elements of nearly 13 400, leading to nearly 334 000 degrees of freedom (recall that quadratic shape functions are used for the displacements). The resulting finite-element mesh is illustrated in the inset in Fig. 7(a). The related computational cost (wall-clock time) of the complete simulation (loading and unloading) varies between 46 hours for the case of uniaxial tension and 27 hours for the case of combined tension–torsion with $\gamma_{\mathrm{f}} = 3.75\%$ (the computations were carried out on a 10-core workstation with Intel Core i7-6950X CPU and 128 GB RAM).

To trigger nucleation of the martensite band, a small imperfection is introduced at the mid-span of the tube, via indenting the surface of the tube by $0.1\,t$ (where t is the tube thickness) over a uniform area, see the inset in Fig. 7(a). The imperfection has been tilted in such a way that a right-handed helical band forms under uniaxial tension, as in the case of combined tension–torsion, when the sense of the twist angle ϕ implies the right-handedness of the helix. Note that, in the case of a symmetric (not tilted) imperfection, the handedness of the helix is random and results from numerical imperfections.

4.2. NiTi tube subjected to uniaxial tension

The case of uniaxial tension is studied first. Figure 8 depicts the snapshots of the transformation pattern during loading together with the nominal axial stress–elongation response. The transformation pattern is represented by the distribution of the volume fraction η shown in the current configuration. The nominal axial stress, denoted by σ, is calculated as the axial force divided by the initial cross-section area.

The martensite band nucleates at the position of the imperfection, see the arrow at snapshot 1 that shows the initial position of the imperfection. Initially, the band has a helical shape with the inclination angle of about 58° with respect to the tube axis, which is in agreement with our previous study (Rezaee-Hajidehi et al., 2020) and with the experiments (Li and Sun, 2002; Feng and Sun, 2006; Reedlunn et al., 2014, 2020a). The type of the martensite band, e.g. a single helix or two symmetric helices, and its handedness are sensitive to the imperfection and boundary conditions, see Jiang et al. (2017b); Rezaee-Hajidehi et al. (2020) for a more detailed discussion.

Formation of the martensite band is accompanied by a stress drop of about 50 MPa, which is slightly higher than the one in the experiment of Sun and Li (2002). The helical band then starts growing in both length and thickness, while the helical angle remains fairly constant, and eventually, in the neighbourhood of point 5 in Fig. 8, it ceases to grow lengthwise with the maximum length (measured along the helix) of about 16.5 mm, which is close to the length of 16 mm observed in the experiment. Subsequently, the band continues to grow in thickness only. It has been observed that

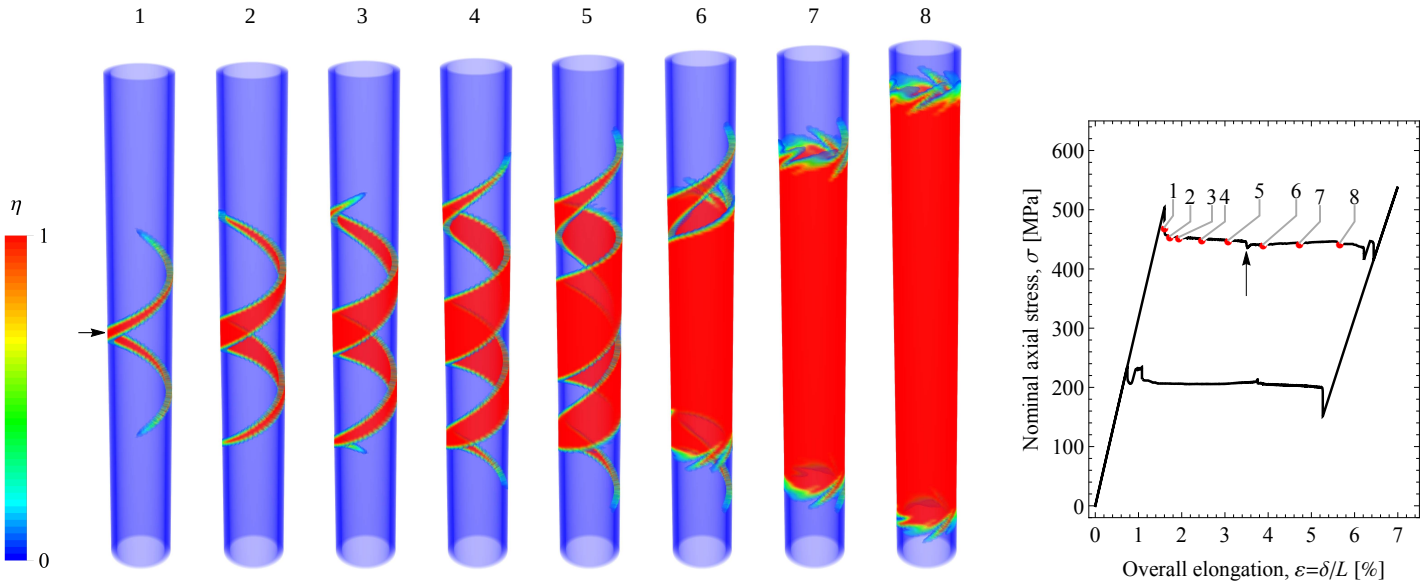

Figure 8: Evolution of the transformation pattern in a NiTi tube subjected to uniaxial tension ($\gamma_f = 0$) and the corresponding nominal axial stress–elongation response.

increasing the height of the tube does not have a significant impact on the transformation pattern. For instance, the maximum length of 17 mm and the inclination angle (at nucleation) of 58° have been obtained for a longer tube with the length $L = 15$ mm.

Between instants 5 and 6 in Fig. 8, the helical martensite domain starts merging into a single cylindrical domain. This event is associated with a stress drop, see the arrow in the nominal axial stress–elongation response. Afterwards, the multi-prong interfaces of the cylindrical domain, see snapshots 7 and 8, propagate simultaneously towards both ends of the tube along helical paths until the tube transforms completely. Such multi-prong fronts have been observed in experiments (Feng and Sun, 2006; Reedlunn et al., 2014, 2020a; Bechle and Kyriakides, 2016), see also the related simulations (Jiang et al., 2017b; Rezaee-Hajidehi et al., 2020; Xiao and Jiang, 2020). The multi-prong fronts have not been reported by Sun and Li (2002), note, however, that their experiment was not accompanied by a full-field measurement of the strain field. The discussion on the impact of the interfacial and elastic strain energy contributions on the competition between multi-prong and ring-shaped interfaces in pseudoelastic tubes can be found in He and Sun (2009).

It can be seen in Fig. 8 that the macroscopic transformation front is, in fact, a diffuse interface separating the domains of austenite and martensite. The thickness of the diffuse interface is relatively small when the interface is inclined, as in the helical band at the initial stage of transformation, while the local interfaces of the multi-prong fronts at the final stage of transformation are visibly thicker. Note that the preferential inclination angle of the helical band ensures geometric compatibility between the transformed domain of martensite and the untransformed domain of

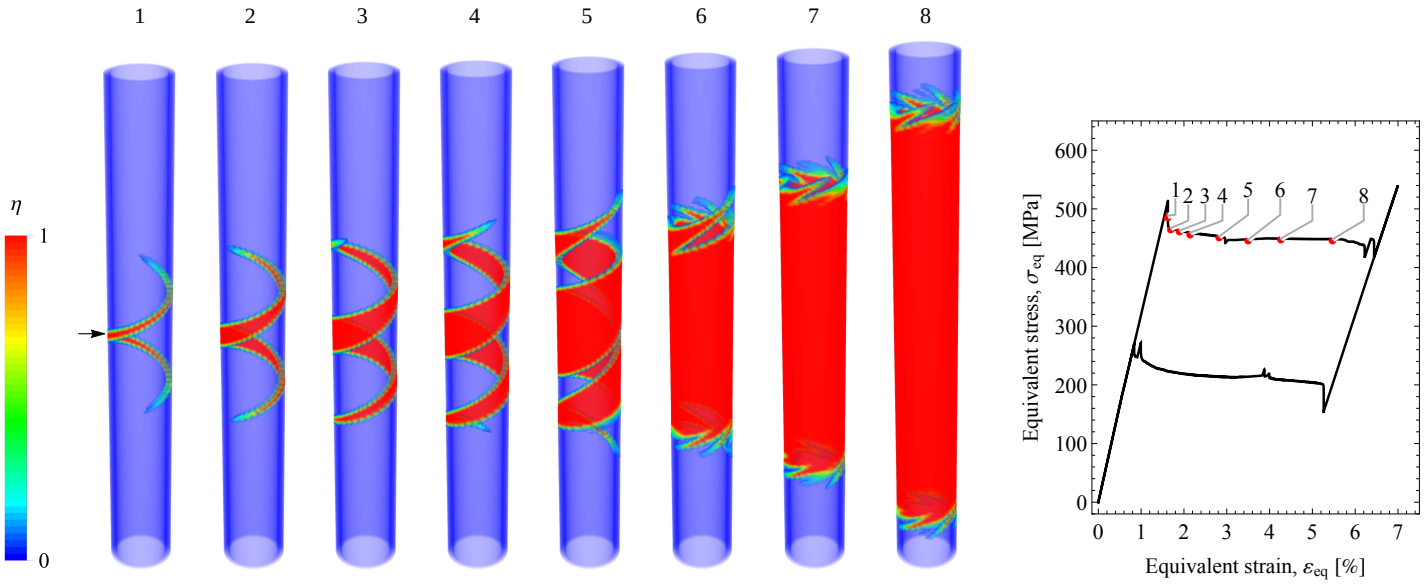

Figure 9: Evolution of the transformation pattern in the NiTi tube subjected to combined tension–torsion and the corresponding equivalent stress–equivalent strain response for the initial torsion $\gamma_f = 0.95\%$.

austenite, see the respective theoretical predictions (Shaw and Kyriakides, 1997a; Li and Sun, 2002; Wendler et al., 2017; Rezaee-Hajidehi et al., 2020) based on the classical analysis of necking-type discontinuity in thin sheets (Nadai, 1950; Hill, 1952). Accordingly, the 3D effects and the related extra energy of the interface are relatively small for a preferentially inclined interface. The 3D effects and the energy of the prong interfaces are higher since the interfaces must accommodate the incompatibility of the transformation strain, and hence their thickness is larger.

The reverse transformation pattern during unloading follows a rather similar evolution as that during loading, see Appendix B. A movie showing the complete transformation pattern evolution for the tube under uniaxial tension is provided as a supplementary material (Movie S1) accompanying this paper.

4.3. NiTi tube subjected to combined tension–torsion

Figures 9–13 show the transformation pattern and the equivalent stress–equivalent strain response of the NiTi tube subjected to tension for different levels of initial torsion γ_f, which is varied between 0.95% and 3.75%. Recall that torsion is applied prior to elongation, and then it is kept constant while the elongation is increased, cf. Fig. 7(b). For the highest initial torsion $\gamma_f = 3.75\%$ studied here, a homogeneous transformation initiates under torsion (with $\eta \approx 0.2$ in the entire volume) already before elongation is applied.

The equivalent stress σ_{eq} and the equivalent strain ε_{eq} are determined according to Eq. (18), the latter evaluated now in terms of the overall strains ε and γ. As in Section 4.2, the nominal axial

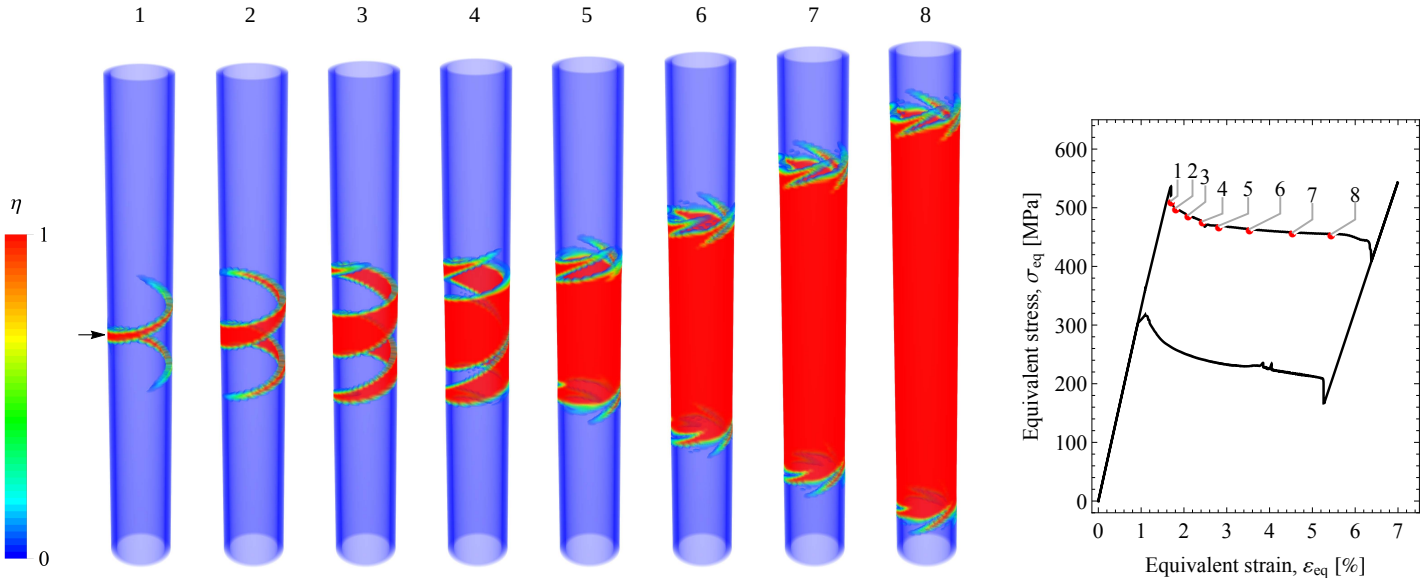

Figure 10: Evolution of the transformation pattern in the NiTi tube subjected to combined tension–torsion and the corresponding equivalent stress–equivalent strain response for the initial torsion $\gamma_f = 1.90\%$.

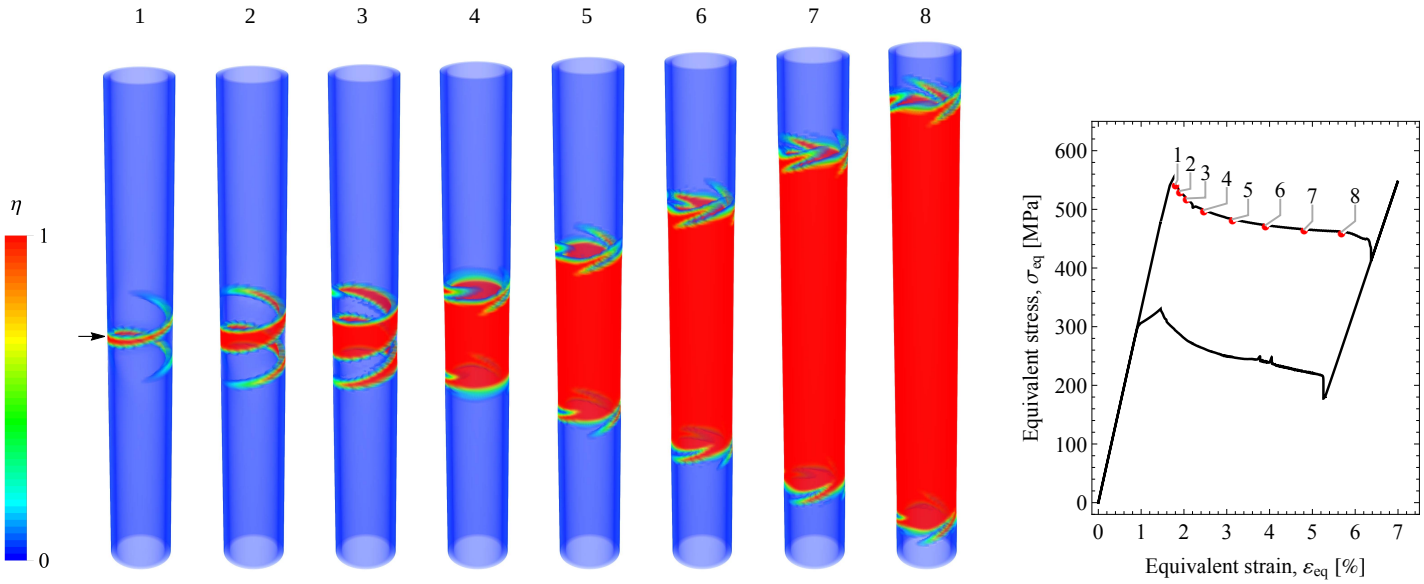

Figure 11: Evolution of the transformation pattern in the NiTi tube subjected to combined tension–torsion and the corresponding equivalent stress–equivalent strain response for the initial torsion $\gamma_f = 2.50\%$.

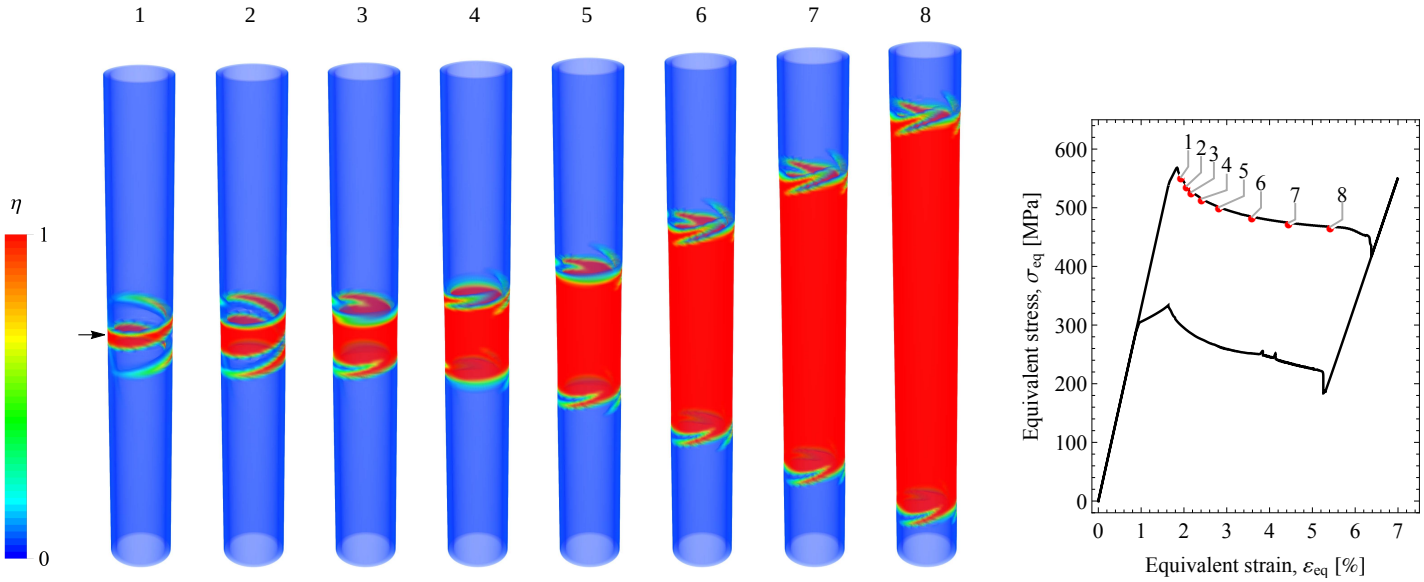

Figure 12: Evolution of the transformation pattern in the NiTi tube subjected to combined tension–torsion and the corresponding equivalent stress–equivalent strain response for the initial torsion $\gamma_f = 2.83\%$.

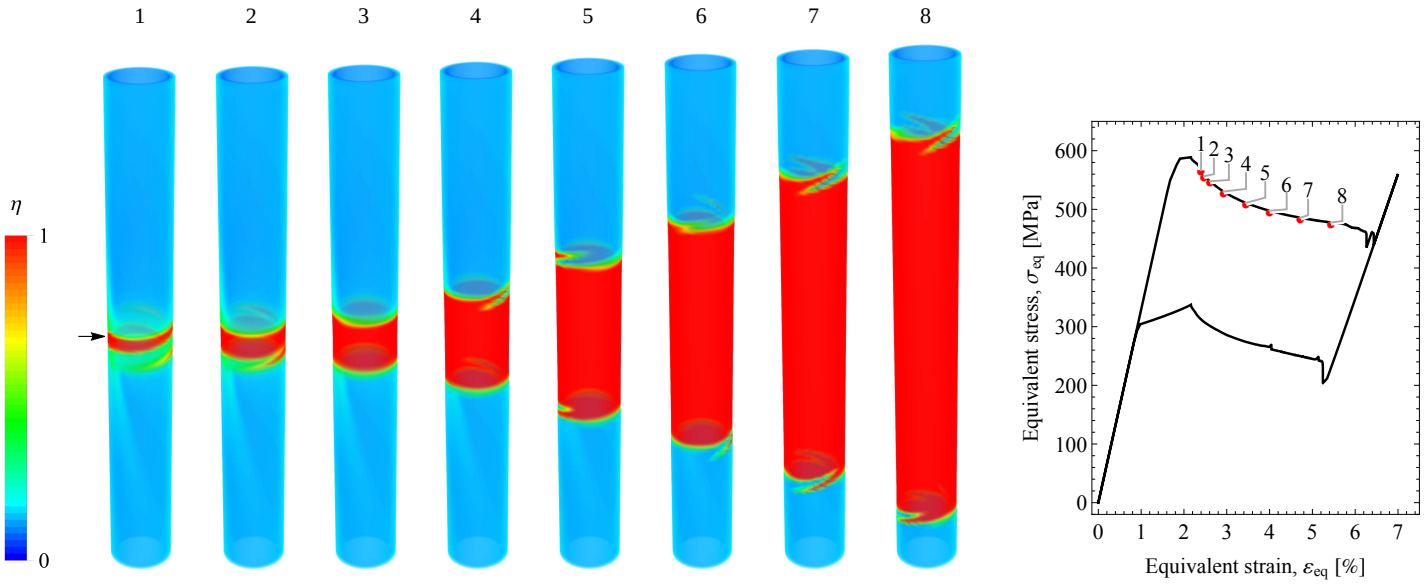

Figure 13: Evolution of the transformation pattern in the NiTi tube subjected to combined tension–torsion and the corresponding equivalent stress–equivalent strain response for the initial torsion $\gamma_f = 3.75\%$.

stress σ is computed as the axial force divided by the initial cross-section area. The nominal shear stress τ is computed as the torque divided by the product of the initial cross-section area and the mean radius.

It can be seen in Figs. 9–13 that in all cases the transformation initiates by nucleation of a helical band that subsequently evolves towards a cylindrical domain with multi-prong fronts. Thus, from this point of view, the transformation pattern is qualitatively similar to that observed in uniaxial tension. The effect of increasing the initial torsion γ_{f} is that the angle of the helical band with respect to the tube axis increases, while the maximum length decreases, i.e. the helical shape evolves towards a ring-like shape. A perfect ring-shaped nucleation band, however, was not observed in the simulations, see snapshots 1 in Figs. 9–13. The maximum band angle and the smallest maximum length are obtained equal to 83° and 7.8 mm, respectively, for $\gamma_{\mathrm{f}} = 3.75\%$. Moreover, it is apparent that, as the size of the helix decreases, it merges into a cylindrical domain at an earlier stage, see e.g. the transformation pattern in Fig. 13 where the cylindrical domain is formed at an early stage of the inhomogeneous transformation. Actually, this is the reason that the computations become cheaper as the value of the initial torsion γ_{f} increases. As discussed above, the prong-like fronts have more diffuse interfaces compared to the preferably-oriented helical bands. Accordingly, propagation of the former proceeds in a computationally more efficient manner, since the mesh can resolve the corresponding interfaces more effectively. Another apparent, yet important, observation from Figs. 9–13 is that, as the value of the initial torsion γ_{f} increases, the number of prongs decreases. For instance, in the case with $\gamma_{\mathrm{f}} = 3.75\%$, only two prongs are formed during propagation of the cylindrical domain, while six prongs are formed in the case of uniaxial tension.

Note that further increase of the initial torsion γ_{f} does not considerably affect the evolution of the transformation pattern, except that the tube is homogeneously transformed to a higher volume fraction of martensite before tension is applied. Besides, the range of γ_{f} examined here is sufficient for the study of the tension–torsion segment of the transformation yield stress locus, which is carried out next. Note also that a complete homogeneous transformation of the tube under torsion could not be obtained, as buckling was observed at the final stage of transformation during loading (our auxiliary study has revealed that this instability results from the specific form of the dissipation potential (5) and the instability is suppressed when a term related to martensite reorientation is included in the dissipation potential).

The reverse transformation during unloading is discussed in Appendix B for two representative cases ($\gamma_{\mathrm{f}} = 1.90\%$ and 2.83%). The corresponding movies showing the complete transformation pattern evolution accompany this paper as a supplementary material (Movies S2 and S3).

To clearly illustrate the transition from a helical band towards a ring-like band, as the initial torsion increases, the shapes of the helical martensite bands are shown in Fig. 14 for different values

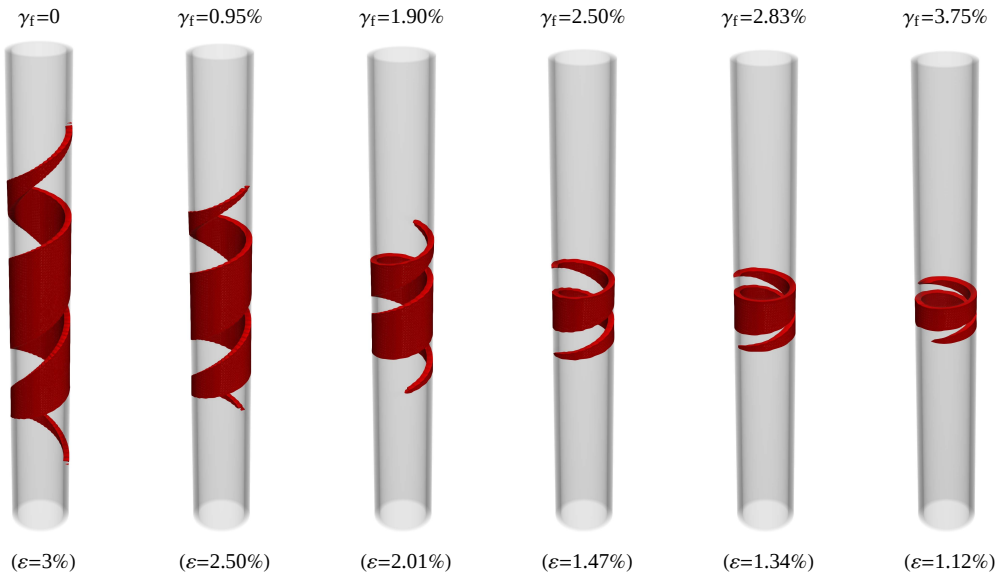

Figure 14: The effect of the initial torsion γ_f on the shape of the helical band at the maximum lengthwise growth. The corresponding overall elongations are given at the bottom.

of γ_f at the respective instants when the helices are at the maximum lengthwise growth. For a more clear visualization, the martensite band is represented by the domain of $\eta \geq 0.5$ so that the diffuseness of the interface is not visible. Moreover, each tube has been rotated about its axis in order to find the most illustrative view of the helix.

Figure 15 shows the helix angles, determined in the reference configuration, at the nucleation stage, see the corresponding snapshots 1 in Figs. 9–13, and at the maximum lengthwise growth of the helical bands, see Fig. 14. The results are compared to the transformation front angles measured by Reedlunn et al. (2020a) separately for the leading and trailing edges, see their Fig. 27(b). To allow comparison, the helix angles are shown as a function of the instantaneous loading angle defined as $\tan^{-1}(\gamma/(2\varepsilon))$ which is analogous to the angle of the proportional strain-space paths used in the experiment. The agreement is good. Note that the evolution of a helical band and its orientation angle at the maximum lengthwise growth (empty markers in Fig. 15) are affected by the loading path (which is here non-proportional, hence the instantaneous loading angle changes). In all cases, the helix angle increases during the band growth, but to a small extent.

The nucleation of the martensite band is always represented by a kink in the equivalent stress–equivalent strain curve, except for the limit case of $\gamma_f = 3.75\%$, where a noticeable homogeneous transformation (with the martensite volume fraction $\eta \approx 0.2$) develops in the tube before initiation of the inhomogeneous transformation under tension, see snapshot 1 in Fig. 13, and thus the nucleation kink is hindered. Note that the tube transforms homogeneously into martensite during torsion also in the case of $\gamma_f = 2.83\%$. However, the related volume fraction is small ($\eta \approx 0.05$) and

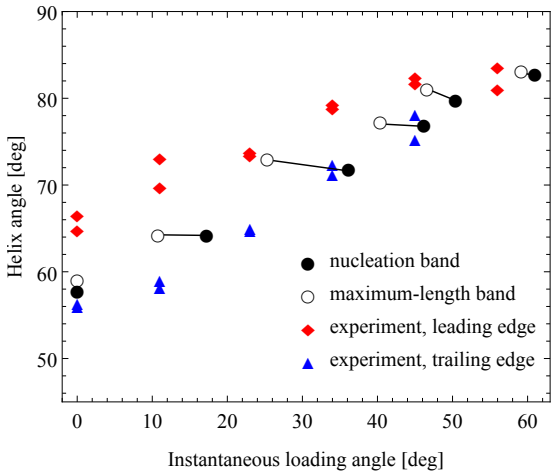

Figure 15: Helix angle at the nucleation and at the maximum lengthwise growth of the helical band as a function of the instantaneous loading angle, $\tan^{-1}(\gamma/(2\varepsilon))$. The markers corresponding to the same initial torsion γ_{f} are joined by a solid line. The predictions are compared to the transformation front angles measured by Reedlunn et al. (2020a).

thus hardly visible in Fig. 12.

It can be seen in Figs. 9–13, see also Fig. 17 below, that, as the initial torsion γ_{f} increases, the equivalent stress at the onset of transformation increases and subsequently the equivalent stress declines more steeply during inhomogeneous transformation. The former stems from the tension–compression asymmetry (controlled by parameter α). The latter, however, is the outcome of the stress redistribution during inhomogeneous transformation under tension. As shown in Fig. 3(b), for $\alpha > 1$, the higher the shear stress, the higher the transformation-onset stresses. In addition, the transformation-onset stress is also influenced by the effect of transverse isotropy (controlled by parameter β), see Fig. 4(b). Figure 16 illustrates the effect of the initial torsion γ_{f} on the shear and axial responses. It can be seen from Fig. 16(a) that the higher the shear stress at the onset of inhomogeneous transformation, the higher the shear stress drop during the inhomogeneous transformation. Figure 17 shows the complete hysteresis loops expressed in terms of the equivalent stress σ_{eq} and equivalent strain $\varepsilon_{\mathrm{eq}}$ for four representative values of γ_{f}.

Using the data provided in Fig. 16(a,b), the transformation yield stress locus of the NiTi tube under combined tension–torsion has been constructed in Fig. 18. The transformation yield stress locus can be determined either in terms of the *overshoot stresses*, indicated by empty triangles in Fig. 16 and corresponding to the instant of the nucleation of the martensite band, or alternatively in terms of the *post-drop stresses*, indicated by filled triangles in Fig. 16 and corresponding to the state just after the abrupt stress drop. On the other hand, in the cases with a smooth transition between the elastic and transformation branches, namely for $\gamma_{\mathrm{f}} = 2.83\%$ and $\gamma_{\mathrm{f}} = 3.75\%$, there is no

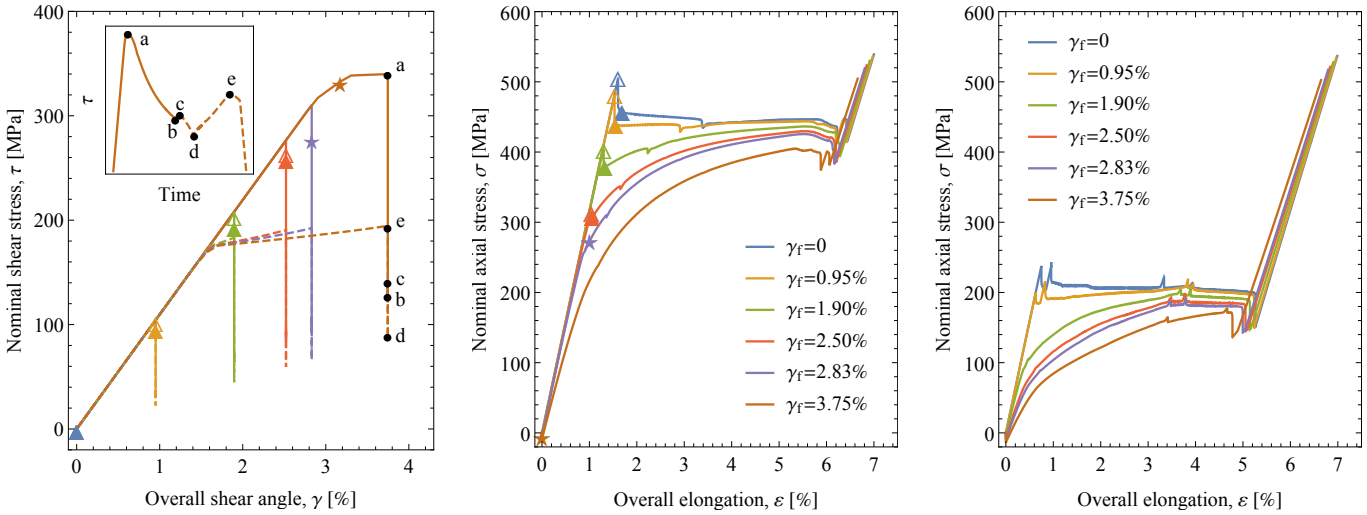

Figure 16: The effect of the initial torsion γ_f on the nominal shear stress–shear angle response (a) and on the nominal axial stress–elongation response during loading (b) and during unloading (c). In the shear response in panel (a), the unloading branches are denoted by dashed lines, and the inset illustrates the non-monotonic evolution of the shear stress τ in time (for selected $\gamma_f = 3.75\%$).

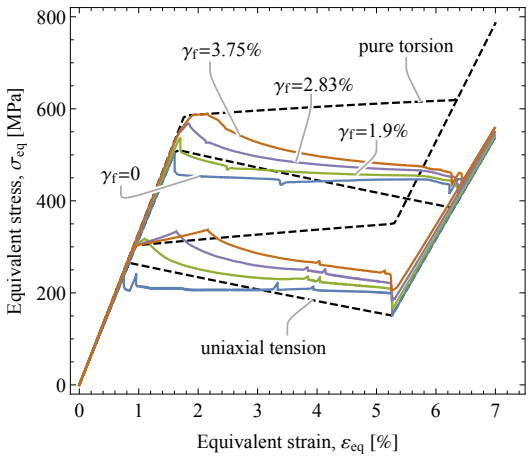

Figure 17: The effect of the initial torsion γ_f on the complete loading–unloading response expressed in terms of the equivalent stress and equivalent strain. The dashed lines represent the intrinsic material responses corresponding to uniaxial tension and pure torsion.

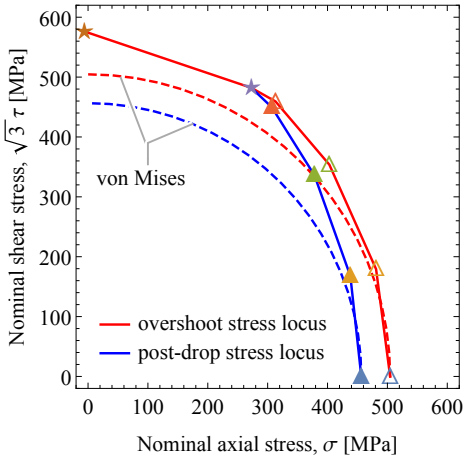

Figure 18: The transformation yield stress locus constructed using the shear and tensile responses of the NiTi tube under combined tension–torsion. The markers refer to those introduced in Fig. 16(a,b).

abrupt nucleation event and no associated stress drop (in the case of $\gamma_f = 2.83\%$, a nucleation kink is noticeable, see Fig. 17, but it is not followed by an abrupt stress drop). The transformation yield stress is then determined at 0.2% offset strain, see the star markers in Fig. 16. Note that the point where the overshoot stress locus intersects the post-drop stress locus indicates the tension–torsion load combination at which the transformation initiation switches between an abrupt nucleation event and a smooth transition.

The von Mises yield stress surfaces are also included in Fig. 18, in order to accentuate the difference between the transformation yield stresses in tension and in torsion that results from the tension–compression asymmetry. Note also that, as illustrated in Fig. 18, the transformation yield surface can be determined in two ways, and each of them leads to a different apparent tension–compression asymmetry. This is discussed in more detail in Section 4.4.

4.4. Study of the transformation yield stress locus in combined tension–torsion

The transformation yield stress locus determined for the NiTi tube undergoing inhomogeneous transformation has been discussed at the end of the previous section, see Fig. 18. Due to the high computational cost, only a few simulations have been performed, and thus the transformation yield stress locus has been identified by a few points only. In this section, the goal is to study the transformation yield stress locus using the material response. Since the computational cost is low, the yield locus can be identified with a higher resolution.

A proportional mixed-control tension–torsion loading is applied, where the engineering axial strain ε and shear angle γ are prescribed, and the resulting nominal axial and shear stresses, respectively, σ and τ are determined. At the same time, all the remaining components of the (Cauchy) stress tensor are enforced to be equal to zero, which corresponds to the stress state in

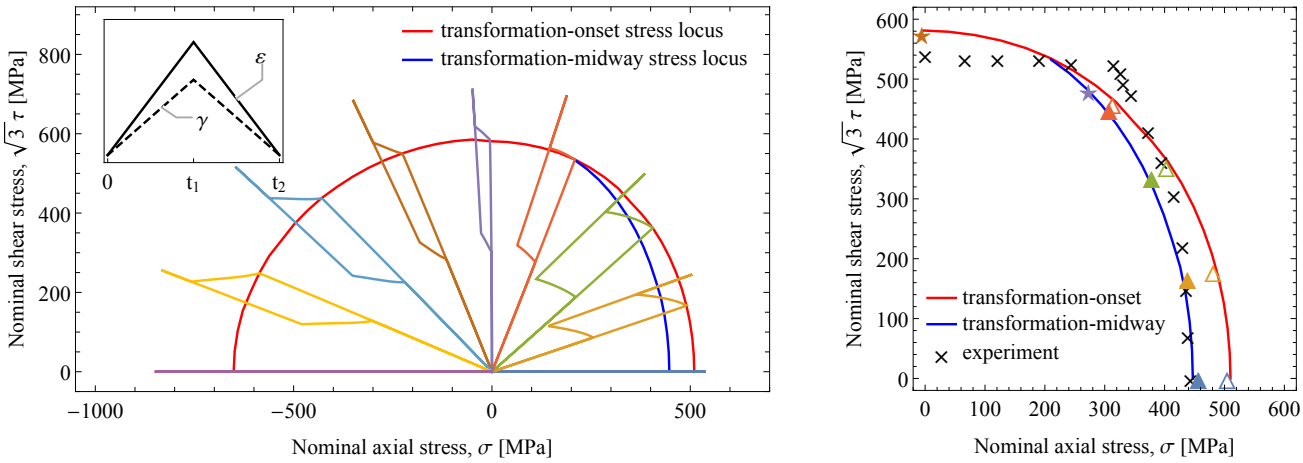

(a) (b)

Figure 19: NiTi under proportional tension–torsion and compression–torsion loading: (a) the complete transformation yield stress locus determined in terms of the intrinsic material response and (b) the tension–torsion segment of the transformation yield stress locus. The proportional loading program is shown as an inset in panel (a). The superimposed color markers and cross markers in panel (b) represent, respectively, the transformation yield stresses obtained in the simulation of the NiTi tube, cf. Figs. 16 and 18, and in the experiment of Sun and Li (2002).

the NiTi tube analyzed previously. The intrinsic material response studied here is free of artifacts such as inhomogeneous deformation due to finite wall thickness and imperfections. As a result, the transformation-onset stresses can be captured with a good precision. In addition, since buckling is not relevant in the material-point study, the analysis is extended to encompass also the compression–torsion loading conditions.

A selected number of (nominal) axial stress–shear stress responses are shown in Fig. 19(a). Despite the proportional loading path, see the inset in Fig. 19(a), the response is not proportional in the stress space, and characteristic hysteresis loops are obtained, except in uniaxial tension and uniaxial compression, where the contribution of the shear stress vanishes. Note that a hysteresis loop is observed also in pure torsion, in which the engineering axial strain ε is constrained to zero, as a result of a compressive axial stress that develops. These qualitative features are consistent with the experimental observations of Helm and Haupt (2003), except for pure torsion in which the hysteresis loop is essentially missing in the experiment. Similar hysteresis loops have also been observed in the recent tension–torsion (e.g., strain path P2) and compression–torsion (e.g., strain paths P11–P14) tests by Reedlunn et al. (2020a), see the corresponding supplemental information (Reedlunn et al., 2020b). Consistent with the experiment is also the development of a compressive axial stress of about 50 MPa in pure torsion, which is due to the Swift effect (Reedlunn et al., 2020a).

Figure 19(a) shows also the transformation yield stress locus determined in terms of the material

response. The respective curves have a smooth appearance, since they have been obtained using a sufficiently large number of loading orientations. In tension-dominated cases, the response in the transformation regime is characterized by a monotonically decreasing equivalent stress. The respective transformation yield stresses can then be represented either by the *transformation-onset stresses* or by the *transformation-midway stresses*. The latter are defined as the stresses at the instant when the volume fraction of martensite is equal to $\eta = 0.5$ and approximately correspond to the post-drop stresses obtained in the case of the NiTi tube, see Fig. 18. The notion of the transformation-midway stress, as defined above, is here close to the classical notion of the Maxwell stress that intersects the non-monotonic material stress–strain response; however, the corresponding Maxwell construction is not immediate in the case of multiaxial loading. On the other hand, the transformation-onset stresses approximately correspond to the overshoot stresses characteristic for the NiTi tube undergoing localized transformation.

In torsion- and compression-dominated cases, where the transformation regime is characterized by a monotonically increasing equivalent stress, the transformation-onset stresses define the transformation yield stress locus in a unique manner, and can be captured precisely on account of the trilinear-like material response.

Figure 19(b) shows an enlarged view of the tension–torsion segment of the transformation yield stress locus. The transformation yield stresses obtained in Section 4.3 and in the experiment of Sun and Li (2002) are superimposed for comparison. It can be recognized from the experimental data reported by Sun and Li (2002) and, in particular, from the experimental curve in Fig. 7(c) that in tension-dominated cases, i.e. when an abrupt nucleation event occurs, the experimental yield stress locus included in Fig. 19(b) has been determined in terms of the post-drop stresses. The overshoot stress, on the other hand, does not provide a reliable measure for the transformation yield stress, as it is very sensitive to the experimental setup, geometry and imperfections (Churchill et al., 2009). Moreover, the overshoot stress is often undetectable in the experiment unless special care is exercised.

Similar to the experiment, the overshoot stresses obtained in the simulation of the NiTi tube, cf. Section 4.3, may exhibit the same sensitivities. However, as shown in Fig. 19(b), the overshoot stress locus obtained here for the NiTi tube, see the empty triangles, agrees well with the transformation-onset stress locus determined in terms of the intrinsic material response. The external factors mentioned earlier appear thus to have a negligible effect on the respective features determined here for the NiTi tube.

It can be seen in Fig. 19 that each of the transformation yield stress loci obtained for NiTi, represents a distinct apparent tension–compression asymmetry. Considering the transformation-onset stresses, the ratio of the yield stress in tension (equal to 510 MPa) to that in compression (equal

to 651 MPa) is equal to 0.78, which is close to $1/\alpha = 0.8$, as expected. Instead, if the transformation-midway stress is taken as the transformation yield stress in tension (equal to 447 MPa), then the corresponding ratio is equal to 0.69, and the apparent tension–compression asymmetry is then much higher. Note that, in experiments, due to the complexities associated with determination of the overshoot stresses (represented here by the transformation-onset stresses), the transformation yield stress locus is usually characterized by means of the post-drop stresses (approximated here by the transformation-midway stresses), and the actual tension–compression asymmetry is determined accordingly. This shows that, regarding the tension–compression asymmetry, care is needed when calibrating the models based on the experimental data, in particular, when the deformation mode is different in tension (strain localization followed by a stress plateau) compared to that in compression or torsion (uniform deformation accompanied by a monotonic stress response). In the present work, the parameter characterizing the tension–compression asymmetry ($\alpha = 1.25$) has been adopted arbitrarily, since our focus here is on qualitative features. Moreover, the post-drop stresses depend also on the hardening parameters H_{T} and H_{C}, see the discussion below, that cannot be easily determined experimentally.

The change of the deformation mode is associated with a corner on the transformation yield locus, cf. Fig. 19, and this qualitative feature is also present, actually even more pronounced, in the experimental locus determined by Sun and Li (2002). Note, however, that the related features are highly sensitive to the way in which the transformation yield stress is determined. In the experiment of Sun and Li (2002), the tension-dominated cases correspond to a non-proportional shear-then-tension loading, while the torsion-dominated cases correspond to a non-proportional tension-then-shear loading, which may influence the resulting yield locus. At the same time, in the recent proportional loading experiments of Reedlunn et al. (2020a), the change of the deformation mode is clearly visible in the overall stress–strain responses (stress plateau under tension-dominated loading vs. smooth and monotonic stress–strain response under torsion dominated loading), but the corner on the transformation yield locus is hardly visible, if present at all. To make the picture even more complex, the transformation under torsion-dominated loading, despite their regular stress–strain response, is accompanied by strain localization along bands approximately aligned with the tube axis, as revealed by full-field DIC measurements (Reedlunn et al., 2020a). This new phenomenon, which currently lacks definite explanation, may also influence the corresponding yield locus.

The post-drop stresses, approximated here by the transformation-midway stresses, significantly depend on the actual softening-like response during transformation, which, in turn, depends on the hardening parameters H_{T} and H_{C}, cf. Eq. (17). The effect of these parameters on the transformation yield stress locus is illustrated in Fig. 20. Note that the transformation-onset stresses do not depend on H_{T} and H_{C}. However, the point at which the transformation-onset and transformation-midway

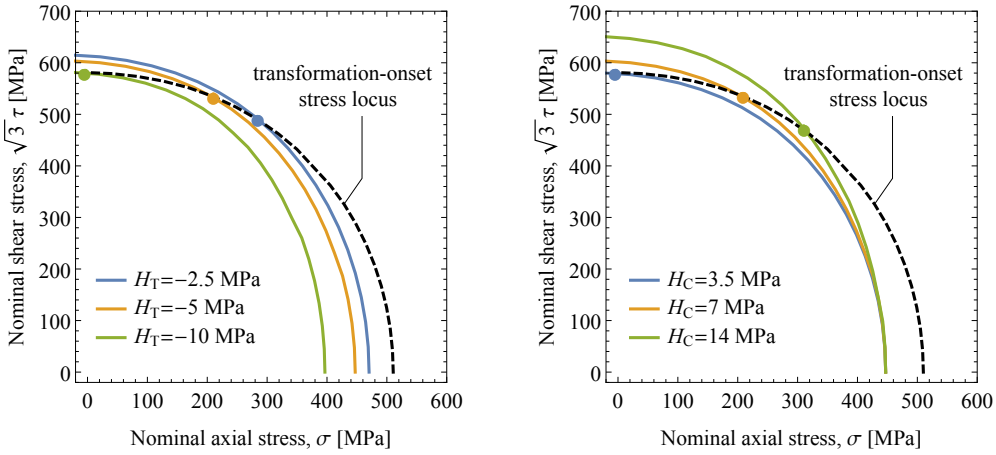

Figure 20: The effect of the hardening parameters H_T (a) and H_C (b) on the transformation-midway stress locus. The dashed line represents the transformation-onset stress locus, which is identical in all cases, and the markers indicate the points at which the transformation-onset stress locus intersects the transformation-midway stress loci.

stress loci intersect does depend on H_T and H_C. This intersection point is indeed an intrinsic feature of the material that emerges from the competition between H_T and H_C, see the markers in Fig. 20. Recall that $H_T = -5$ MPa and $H_C = 7$ MPa are the baseline values that were used in the preceding simulations. It can be observed that, as the absolute value of H_T increases, the intersection point approaches the pure torsion axis, i.e. a wider range of the responses are characterized by softening. This is also accompanied by a decrease of the transformation-midway stress in uniaxial tension. The intersection point moves towards the pure torsion axis also when parameter H_C is decreased. At the same time, the transformation-midway stress in uniaxial tension does not depend on H_C.

5. Conclusion

Propagating instabilities and the related transformation patterns in NiTi tubes subjected to combined tension–torsion have been studied, apparently for the first time, using a recently developed finite-strain gradient-enhanced model of pseudoelasticity (Rezaee-Hajidehi et al., 2020). The model is capable of capturing the complex features observed in the experiment by Sun and Li (2002) which has been taken as the reference (and motivation) for the present study. The major experimental effect that has been correctly reproduced is that the transformation is inhomogeneous for tension-dominated loading and homogeneous for torsion-dominated loading. Furthermore, the predicted pattern of inhomogeneous transformation is that of a helical martensite band that upon subsequent loading merges into a cylindrical domain with multi-prong transformation fronts, in qualitative agreement with the experimental observations (Reedlunn et al., 2020a). It has been also shown

that, as the initial torsion is increased, the inclination angle of the helical band with respect to the tube axis increases, while its maximum length decreases.

It is well recognized that inhomogeneity of transformation results from a non-monotonic (up-down-up) intrinsic stress–strain response which is typical for NiTi under tension and which can be easily included in the constitutive model. Crucial for describing the change in the deformation mode (from inhomogeneous to homogeneous) is that the stress–strain response becomes monotonic under torsion. It follows that such a constitutive behaviour (non-monotonic response in tension and monotonic in torsion) can be achieved for physically-relevant model parameters only if the model includes the following three features, namely the tension–compression asymmetry, transverse isotropy of the transformation strain, and deformation-dependent hardening/softening behaviour.

The present results lead also to an important observation concerning the apparent transformation yield stress locus. In tension-dominated cases, when the overall pseudoelastic response is characterized by a stress drop followed by a stress plateau, the yield stress locus can be determined in two different ways, namely in terms of the overshoot stresses or in terms of the post-drop stresses, and each of them yields a different apparent tension–compression asymmetry. In the experimental practice, the yield stress locus would be typically determined in terms of the post-drop stresses, since the overshoot stresses are highly sensitive to experimental conditions and sometimes are not even observed. It follows that care is needed when interpreting the experimental data regarding the asymmetry of the transformation yield stresses in tension and compression, as the two may be represented by quantities of different nature. It seems that the related ambiguity has been overlooked in the literature to date.

Appendix A. Determination of the transformation-onset stresses

In this appendix, we describe the procedure used in Section 2.4 for the determination of the transformation-onset stresses. The analysis concerns the material-point response, hence the gradient term ϕ_{grad} in the Helmholtz free energy function is not considered. To simplify the analysis, the small-strain version of the model is employed.

In analogy to Eq. (3), the local Helmholtz free energy function in the small-strain setting is adopted as

$$\phi(\boldsymbol{\varepsilon}, \bar{\boldsymbol{\varepsilon}}^{\mathrm{t}}, \eta) = \phi_0^{\mathrm{a}} + \Delta\phi_0\eta + \mu\,\mathrm{tr}(\boldsymbol{\varepsilon}_{\mathrm{dev}}^{\mathrm{e}})^2 + \frac{1}{2}\kappa(\mathrm{tr}\,\boldsymbol{\varepsilon}^{\mathrm{e}})^2 + \frac{1}{2}H\eta^2, \qquad \boldsymbol{\varepsilon} = \boldsymbol{\varepsilon}^{\mathrm{e}} + \eta\bar{\boldsymbol{\varepsilon}}^{\mathrm{t}}, \tag{A.1}$$

where $\boldsymbol{\varepsilon}$ is the strain tensor that is additively decomposed into elastic and transformation parts $\boldsymbol{\varepsilon}^{\mathrm{e}}$ and $\eta\bar{\boldsymbol{\varepsilon}}^{\mathrm{t}}$, respectively, and $\bar{\boldsymbol{\varepsilon}}^{\mathrm{t}}$ is the limit transformation strain, i.e. the counterpart of $\bar{\boldsymbol{e}}^{\mathrm{t}}$ in the finite-strain model. The model is further simplified by assuming an identical shear modulus for austenite and martensite $\mu_{\mathrm{a}} = \mu_{\mathrm{m}} = \mu$ as well as a constant interaction coefficient H.

Upon prescribing the total strain $\boldsymbol{\varepsilon}$, the limit transformation strain $\bar{\boldsymbol{\varepsilon}}^{\mathrm{t}}$ and the volume fraction η are determined by minimizing the local incremental potential $\pi = \pi(\boldsymbol{\varepsilon}, \bar{\boldsymbol{\varepsilon}}^{\mathrm{t}}, \eta)$ in its small-strain non-gradient version, cf. Eqs. (26)–(27). During the forward transformation, the necessary condition for the minimum of π with respect to η is expressed in the following form (Rezaee-Hajidehi and Stupkiewicz, 2018),

$$f_\eta = f_{\mathrm{c}}, \qquad f_\eta = -\frac{\partial \phi}{\partial \eta} = -\Delta\phi_0 + \mathrm{tr}(\boldsymbol{\sigma} \cdot \bar{\boldsymbol{\varepsilon}}^{\mathrm{t}}) - H\eta, \tag{A.2}$$

where f_η is the thermodynamic driving force conjugate to η, and $\boldsymbol{\sigma}$ denotes the stress tensor.

On the other hand, minimization of π with respect to $\bar{\boldsymbol{\varepsilon}}^{\mathrm{t}}$ is performed by adopting a Lagrange function $L = \phi + \eta\,\omega\, g(\bar{\boldsymbol{\varepsilon}}^{\mathrm{t}})$, where the Lagrange multiplier ω is used to impose the equality constraint $g(\bar{\boldsymbol{\varepsilon}}^{\mathrm{t}}) = 0$ that is introduced in π through the indicator function $I_{\bar{\mathcal{P}}}$, cf. Eq. (7). The condition of stationarity of L with respect to $\bar{\boldsymbol{\varepsilon}}^{\mathrm{t}}$ can be written in the following form,

$$\mathbf{0} = \frac{\partial L}{\partial \bar{\boldsymbol{\varepsilon}}^{\mathrm{t}}} = \frac{\partial \phi}{\partial \bar{\boldsymbol{\varepsilon}}^{\mathrm{t}}} + \eta\,\omega\,\frac{\partial g}{\partial \bar{\boldsymbol{\varepsilon}}^{\mathrm{t}}} = \eta(-\boldsymbol{\sigma}_{\mathrm{dev}} + \omega\frac{\partial g}{\partial \bar{\boldsymbol{\varepsilon}}^{\mathrm{t}}}), \tag{A.3}$$

which implies that the deviatoric stress $\boldsymbol{\sigma}_{\mathrm{dev}}$ is normal to the surface of the limit transformation strain $g(\bar{\boldsymbol{\varepsilon}}^{\mathrm{t}}) = 0$ (recall that $\bar{\boldsymbol{\varepsilon}}^{\mathrm{t}}$ is a deviator on account of the assumption of isochoric transformation).

Consider now a material point subjected to the stress state specified by a unit deviator $\bar{\boldsymbol{\sigma}}_{\mathrm{dev}}$, $\|\bar{\boldsymbol{\sigma}}_{\mathrm{dev}}\| = 1$. With reference to the stationarity condition (A.3), and considering the onset of transformation so that $\eta \to 0$, the following set of equations is obtained,

$$\begin{cases} -\bar{\boldsymbol{\sigma}}_{\mathrm{dev}} + \bar{\omega}\dfrac{\partial g(\bar{\boldsymbol{\varepsilon}}^{\mathrm{t}})}{\partial \bar{\boldsymbol{\varepsilon}}^{\mathrm{t}}} = \mathbf{0}, \\ g(\bar{\boldsymbol{\varepsilon}}^{\mathrm{t}}) = 0, \end{cases} \tag{A.4}$$

where $\bar{\omega}$ is a scaled Lagrange multiplier that corresponds to the unit tensor $\bar{\boldsymbol{\sigma}}_{\mathrm{dev}}$.

The set of equations (A.4) involves 6 independent equations and 6 unknowns, i.e. 5 components of the deviatoric limit transformation strain $\bar{\boldsymbol{\varepsilon}}^{\mathrm{t}}$ and the Lagrange multiplier $\bar{\omega}$. After solving equations (A.4), the deviatoric part $\boldsymbol{\sigma}^{\mathrm{t}}_{\mathrm{dev}}$ of the transformation-onset stress tensor $\boldsymbol{\sigma}^{\mathrm{t}}$ is determined by scaling the unit tensor $\bar{\boldsymbol{\sigma}}_{\mathrm{dev}}$, namely $\boldsymbol{\sigma}^{\mathrm{t}}_{\mathrm{dev}} = s\bar{\boldsymbol{\sigma}}_{\mathrm{dev}}$, where the scaling factor s is found such that the transformation criterion (A.2) is satisfied for $\eta \to 0$. The spherical part of $\boldsymbol{\sigma}^{\mathrm{t}}$ can then be determined according to the desired stress state, e.g., biaxial loading.

Appendix B. Reverse transformation pattern during unloading

Reverse transformation patterns during unloading are reported in this appendix for three representative cases of the NiTi tube under uniaxial tension (Section 4.2) and under combined tension–torsion for the initial torsion $\gamma_{\mathrm{f}} = 1.90\%$ and 2.83% (Section 4.3).

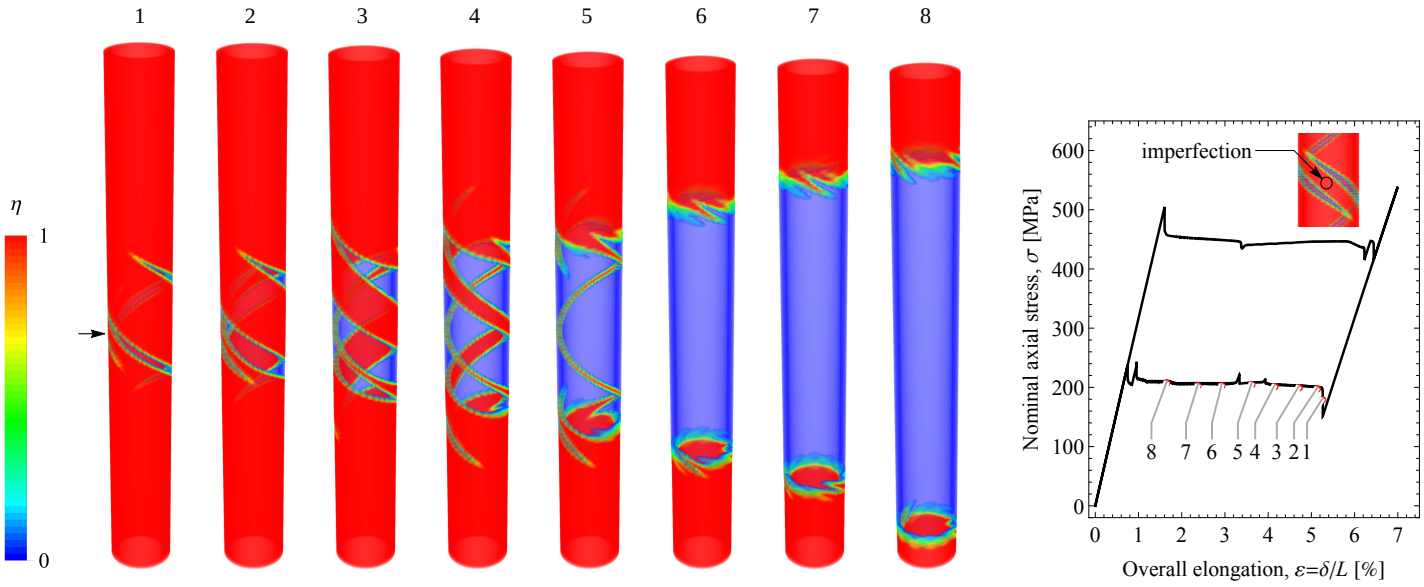

Figure B.1: Evolution of the reverse transformation pattern during unloading in a NiTi tube subjected to uniaxial tension ($\gamma_f = 0$) and the corresponding nominal axial stress–elongation response.

In the case of uniaxial tension, the reverse transformation follows a rather similar evolution as that of the forward transformation during loading, see Fig. B.1. Specifically, a helix-to-cylinder conversion of the austenitic domain is observed. However, the reverse transformation initiates by the nucleation of two (left-handed) helical bands both inclined at about 63° with respect to the tube axis and mirrored to each other with respect to the imperfection position, see the inset in Fig. B.1. Afterwards, the two helices grow simultaneously and merge into a single cylindrical domain of austenite with multi-prong fronts which concurrently (but not synchronously) travel towards the ends of the tube. It can be seen that the fronts of the cylindrical austenite domain during the reverse transformation are more diffuse and less apparent compared to those of the cylindrical martensite domain during forward transformation, cf. Fig 8.

The reverse transformation during unloading for $\gamma_f = 1.90\%$ and 2.83% is illustrated in Figs. B.2 and B.3, respectively. In both cases, similar to the uniaxial tension case, Fig. B.1, the transformation initiates by formation of two left-handed helices, which are inclined with respect to the tube axis at about 61° and 58°, respectively, for $\gamma_f = 1.90\%$ and 2.83%, followed by merging of the helices into a single cylindrical austenite domain with multi-prong fronts. Interestingly, after formation of the cylindrical domain, the handedness of the prongs alters from left-handed to right-handed, see the arrows in the equivalent stress–equivalent strain responses in Figs. B.2 and B.3 pointing towards the corresponding instants. Note that due to the large diffuseness of the fronts, ring-shaped interfaces are formed at the final stage of unloading for the case with $\gamma_f = 2.83\%$, see snapshots 7 and 8 in Fig. B.3.

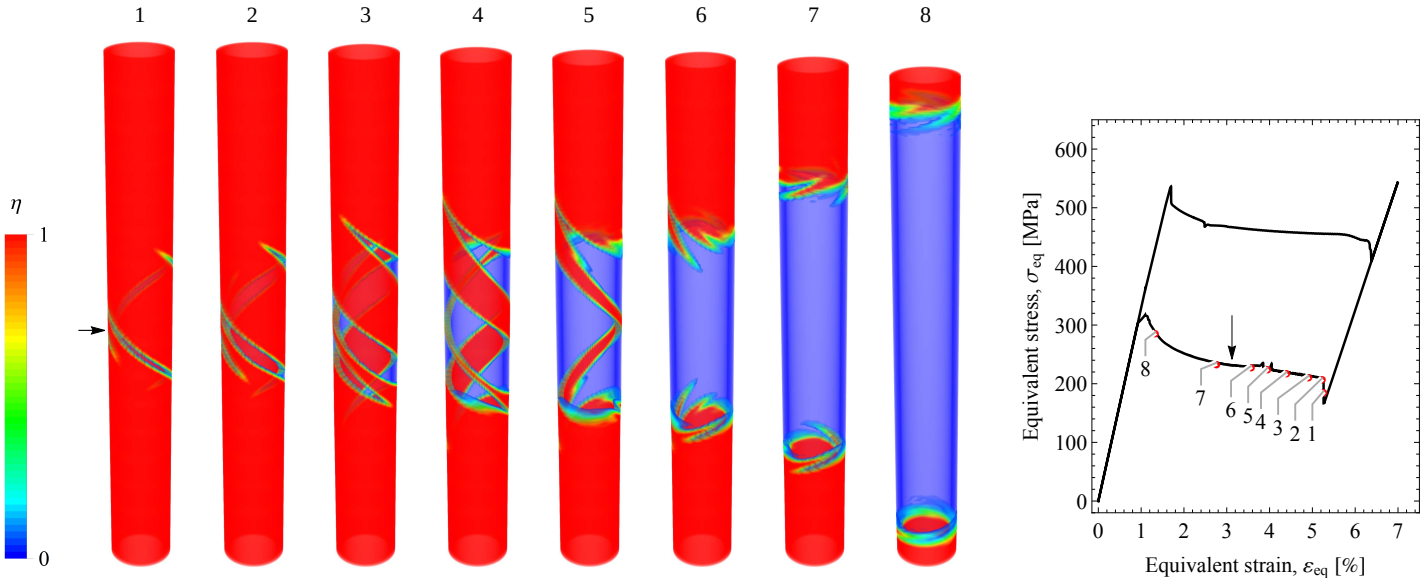

Figure B.2: Evolution of the reverse transformation pattern during unloading in a NiTi tube subjected to combined tension–torsion and the corresponding equivalent stress–equivalent strain response for the initial torsion $\gamma_f = 1.90\%$.

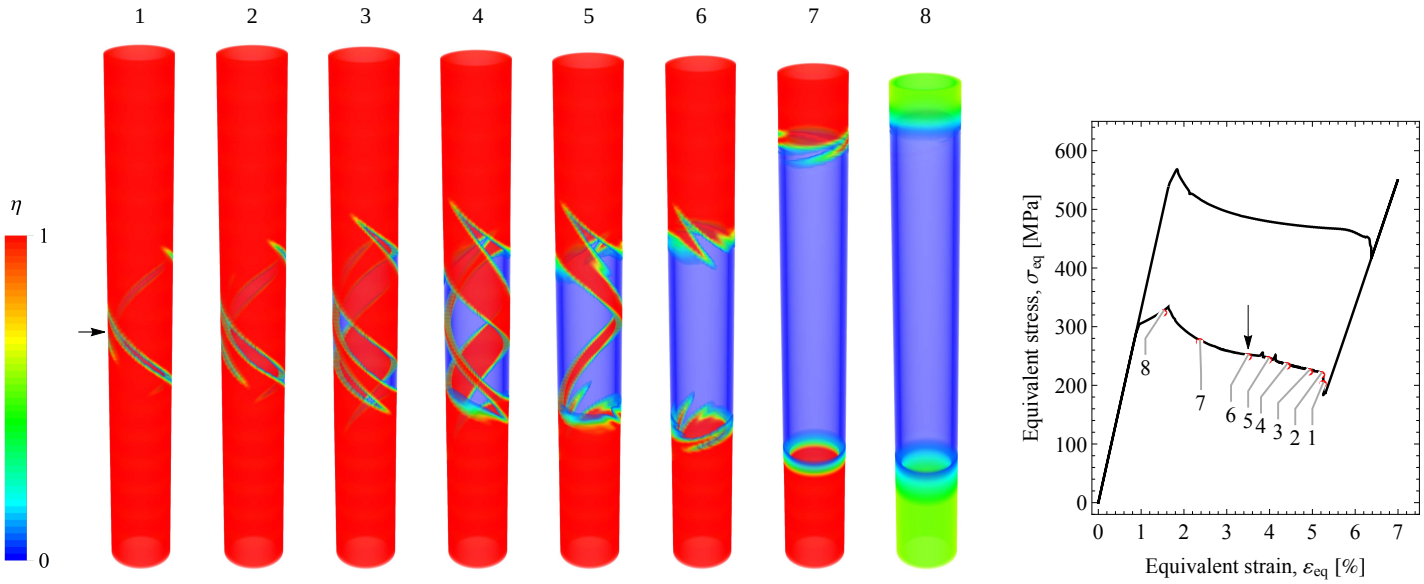

Figure B.3: Evolution of the reverse transformation pattern during unloading in a NiTi tube subjected to combined tension–torsion and the corresponding equivalent stress–equivalent strain response for the initial torsion $\gamma_f = 2.83\%$.

Acknowledgement. This work has been partially supported by the National Science Center (NCN) in Poland through Grant No. 2018/29/B/ST8/00729. The authors thank the anonymous reviewers for their most helpful comments.

References

Alarcon, E., Heller, L., Arbab Chirani, S., Šittner, P., Kopeček, J., Saint-Sulpice, L., Calloch, S., 2017. Fatigue performance of superelastic NiTi near stress-induced martensitic transformation. Int. J. Fatigue 95, 76–89.

Alessi, R., Bernardini, D., 2015. Analysis of localization phenomena in Shape Memory Alloys bars by a variational approach. Int. J. Solids Struct. 73, 113–133.

Badnava, H., Kadkhodaei, M., Mashayekhi, M., 2014. A non-local implicit gradient-enhanced model for unstable behaviors of pseudoelastic shape memory alloys in tensile loading. Int. J. Solids Struct. 51, 4015–4025.

Bechle, N.J., Kyriakides, S., 2014. Localization in NiTi tubes under bending. Int. J. Solids Struct. 51, 967–980.

Bechle, N.J., Kyriakides, S., 2016. Evolution of localization in pseudoelastic NiTi tubes under biaxial stress states. Int. J. Plast. 82, 1–31.

Bhattacharya, K., 2003. Microstructure of martensite: why it forms and how it gives rise to the shape-memory effect. Oxford University Press, Oxford.

Chang, B.C., Shaw, J.A., Iadicola, M.A., 2006. Thermodynamics of shape memory alloy wire: modeling, experiments, and application. Continuum Mech. Thermodyn. 18, 83–118.

Churchill, C.B., Shaw, J.A., Iadicola, M.A., 2009. Tips and tricks for characterizing shape memory alloy wire: Part 3—Localization and propagation phenomena. Exp. Tech. 33, 70–78.

Duval, A., Haboussi, M., Ben Zineb, T., 2011. Modelling of localization and propagation of phase transformation in superelastic SMA by a gradient nonlocal approach. Int. J. Solids Struct. 48, 1879–1893.

Feng, P., Sun, Q.P., 2006. Experimental investigation on macroscopic domain formation and evolution in polycrystalline NiTi microtubing under mechanical force. J. Mech. Phys. Solids 54, 1568–1603.

Forest, S., 2009. Micromorphic approach for gradient elasticity, viscoplasticity, and damage. J. Eng. Mech. 135, 117–131.

Frost, M., Benešová, B., Seiner, H., Kružík, M., Šittner, P., Sedlák, P., 2020. Thermomechanical model for NiTi-based shape memory alloys covering macroscopic localization of martensitic transformation. Int. J. Solids Struct. doi:10.1016/j.ijsolstr.2020.08.012.

Grabe, C., Bruhns, O.T., 2008. Tension/torsion tests of pseudoelastic, polycrystalline NiTi shape memory alloys under temperature control. Mat. Sci. Engng. A 481, 109–113.

Grabe, C., Bruhns, O.T., 2009. Path dependence and multiaxial behavior of a polycrystalline NiTi alloy within the pseudoelastic and pseudoplastic temperature regimes. Int. J. Plast. 25, 513–545.

Hallai, J.F., Kyriakides, S., 2013. Underlying material response for Lüders-like instabilities. Int. J. Plast. 47, 1–12.

He, Y.J., Sun, Q.P., 2009. Effects of structural and material length scales on stress-induced martensite macro-domain patterns in tube configurations. Int. J. Solids Struct. 46, 3045–3060.

He, Y.J., Sun, Q.P., 2010. Macroscopic equilibrium domain structure and geometric compatibility in elastic phase transition of thin plates. Int. J. Mech. Sci. 52, 198–211.

Helm, D., Haupt, P., 2003. Shape memory behaviour: modelling within continuum thermomechanics. Int. J. Solids Struct. 40, 827–849.

Hill, R., 1952. On discontinuous plastic states, with special reference to localized necking in thin sheets. J. Mech. Phys. Solids 1, 19–30.

Holzapfel, G.A., 2006. Nonlinear Solid Mechanics. Wiley, Chichester.

Jiang, D., Kyriakides, S., Bechle, N.J., Landis, C.M., 2017a. Bending of pseudoelastic NiTi tubes. Int. J. Solids Struct. 124, 192–214.

Jiang, D., Kyriakides, S., Landis, C.M., 2017b. Propagation of phase transformation fronts in pseudoelastic NiTi tubes under uniaxial tension. Extreme Mech. Lett. 15, 113–121.

Jiang, D., Kyriakides, S., Landis, C.M., Kazinakis, K., 2017c. Modeling of propagation of phase transformation fronts in NiTi under uniaxial tension. Eur. J. Mech. A/Solids 64, 131–142.

Korelc, J., 2009. Automation of primal and sensitivity analysis of transient coupled problems. Comp. Mech. 44, 631–649.

Korelc, J., Wriggers, P., 2016. Automation of Finite Element Methods. Springer International Publishing, Switzerland.

Lexcellent, C., Blanc, P., 2004. Phase transformation yield surface determination for some shape memory alloys. Acta Mater. 52, 2317–2324.

Li, Z.Q., Sun, Q.P., 2002. The initiation and growth of macroscopic martensite band in nano-grained NiTi microtube under tension. Int. J. Plast. 18, 1481–1498.

Lim, T.J., McDowell, D.L., 1999. Mechanical behavior of an Ni-Ti shape memory alloy under axial-torsional proportional and nonproportional loading. J. Eng. Mater. Tech. 121, 9–18.

Mao, S.C., Luo, J.F., Zhang, Z., Wu, M.H., Liu, Y., Han, X.D., 2010. EBSD studies of the stress-induced B2–B19′ martensitic transformation in NiTi tubes under uniaxial tension and compression. Acta Mater. 58, 3357–3366.

Mazière, M., Forest, S., 2015. Strain gradient plasticity modeling and finite element simulation of Lüders band formation and propagation. Continuum Mech. Thermodyn. 27, 83–104.

McNaney, J.M., Imbeni, V., Jung, Y., Papadopoulos, P., Ritchie, R., 2003. An experimental study of the superelastic effect in a shape-memory Nitinol alloy under biaxial loading. Mech. Mat. 35, 969–986.

Nadai, A., 1950. Theory of flow and fracture of solids, Vol 1, 2nd Edition. McGraw-Hill, New York.

Orgéas, L., Favier, D., 1998. Stress-induced martensitic transformation of a NiTi alloy in isothermal shear, tension and compression. Acta Mater. 46, 5579–5591.

Pieczyska, E., Gadaj, S., Nowacki, W., Tobushi, H., 2006. Phase-transformation fronts evolution for stress-and strain-controlled tension tests in TiNi shape memory alloy. Exp. Mech. 46, 531–542.

Reedlunn, B., Churchill, C.B., Nelson, E.E., Shaw, J.A., Daly, S.H., 2014. Tension, compression, and bending of superelastic shape memory alloy tubes. J. Mech. Phys. Solids 63, 506–537.

Reedlunn, B., LePage, W.S., Daly, S.H., Shaw, J.A., 2020a. Axial-torsion behavior of superelastic tubes: Part I, proportional isothermal experiments. Int. J. Solids Struct. 199, 1–35.

Reedlunn, B., LePage, W.S., Daly, S.H., Shaw, J.A., 2020b. Raw data, supplemental plots, and videos for 'Axial-torsion behavior of superelastic tubes: Part I, proportional isothermal experiments'. doi:10.17632/rsfg5474tr.1.

Rezaee-Hajidehi, M., Stupkiewicz, S., 2018. Gradient-enhanced model and its micromorphic regularization for simulation of Lüders-like bands in shape memory alloys. Int. J. Solids Struct. 135, 208–218.

Rezaee-Hajidehi, M., Tůma, K., Stupkiewicz, S., 2020. Gradient-enhanced thermomechanical 3D model for simulation of transformation patterns in pseudoelastic shape memory alloys. Int. J. Plast. 128, 102589.

Ryś, M., Forest, S., Petryk, H., 2020. A micromorphic crystal plasticity model with the gradient-enhanced incremental hardening law. Int. J. Plast. 128, 102655.

Sadjadpour, A., Bhattacharya, K., 2007. A micromechanics-inspired constitutive model for shape-memory alloys. Smart Mater. Struct. 16, 1751.

Sedlák, P., Frost, M., Benešová, B., Zineb, T.B., Šittner, P., 2012. Thermomechanical model for NiTi-based shape memory alloys including R-phase and material anisotropy under multi-axial loadings. Int. J. Plast. 39, 132–151.

Shaw, J.A., Kyriakides, S., 1997a. Initiation and propagation of localized deformation in elasto-plastic strips under uniaxial tension. Int. J. Plast. 13, 837–871.

Shaw, J.A., Kyriakides, S., 1997b. On the nucleation and propagation of phase transformation fronts in a NiTi alloy. Acta Mater. 45, 683–700.

Stupkiewicz, S., Petryk, H., 2010. A bi-crystal aggregate model of pseudoelastic behaviour of shape-memory alloy polycrystals. Int. J. Mech. Sci. 52, 219–228.

Stupkiewicz, S., Petryk, H., 2013. A robust model of pseudoelasticity in shape memory alloys. Int. J. Num. Meth. Engng. 93, 747–769.

Stupkiewicz, S., Rezaee-Hajidehi, M., Petryk, H., 2020. Multiscale analysis of the effect of interfacial energy on non-monotonic stress-strain response in shape memory alloys. Int. J. Solids Struct. doi:10.1016/j.ijsolstr.2020.04.006.

Sun, Q.P., Li, Z.Q., 2002. Phase transformation in superelastic NiTi polycrystalline micro-tubes under tension and torsion—from localization to homogeneous deformation. Int. J. Solids Struct. 39, 3797–3809.

Thamburaja, P., Anand, L., 2001. Polycrystalline shape-memory materials: effect of crystallographic texture. J. Mech. Phys. Solids 49, 709–737.

Wang, X.M., Wang, Y.F., Lu, Z.Z., Deng, C., Yue, Z.F., 2010. An experimental study of the superelastic behavior in NiTi shape memory alloys under biaxial proportional and non-proportional cyclic loadings. Mech. Mat. 42, 365–373.

Wendler, F., Ossmer, H., Chluba, C., Quandt, E., Kohl, M., 2017. Mesoscale simulation of elastocaloric cooling in SMA films. Acta Mater. 136, 105–117.

Xiao, Y., Jiang, D., 2020. Rate dependence of transformation pattern in superelastic NiTi tube. Extreme Mech. Lett. , 100819.

Zhang, X., Feng, P., He, Y., Yu, T., Sun, Q.P., 2010. Experimental study on rate dependence of macroscopic domain and stress hysteresis in NiTi shape memory alloy strips. Int. J. Mech. Sci. 52, 1660–1670.